Engineering and Computational Mechanics
Volume - Issue -

Proceedings of the Institution of Civil Engineers
Pages 1–30

Keywords: Large-Eddy Simulation, Wind Loading, CAARC building, Rectangular Cylinders, Vortex-Induced Vibration, Freestream Turbulence

ice | proceedings

An overview of Large-Eddy Simulation for wind loading on slender structures

Steven J. Daniels PhD
Research Fellow, College of Engineering, Mathematics and Physical Sciences, University of Exeter, Harrison Building, Streatham Campus, North Park Road, Exeter, EX4 4QF, UK.
(corresponding author: S.Daniels@exeter.ac.uk)

Zheng-Tong Xie PhD
Associate Professor, Aeronautics and Astronautics, Faculty of Engineering and the Environment, Highfield Campus, University of Southampton, Southampton, SO17 1BJ, UK.

Understanding and predicting the effects of wind loading on a structure is necessary for a safe, effective, and economical engineering design. Wind tunnel techniques are expensive and often provide data that is not sufficiently detailed for the structural engineer. With increasing advances in computational capabilities, it has recently become feasible to investigate these flows using numerical techniques. Of these, one of the most effective approaches to simulate the turbulence observed in natural wind is Large-Eddy Simulation (LES). The application of LES to analyse wind loading, and aeroelastic effects on structures are only a recent venture in the field. This paper reviews the progress made over the last few decades for the analysis of wind flow around slender structures, and the more recent analysis incorporating the effects of freestream turbulence. Firstly, a review of the literature for generating freestream turbulence is carried out, and are assessed based on their flaws and strengths. A number of these are subsequently used for the analysis of surface pressures on an isolated tall model building. Subsequently, a review is made into wind tunnel analysis and LES for the aeroelastic analysis of bridge sections. The recent advances in the understanding of turbulence effects on the aeroestatic responses are summarised. The future of LES and its relationship wind tunnel analysis for wind loading analysis are discussed.

1. Introduction

The new generation of civil engineering structures are tending towards taller and more slender designs, while concurrently their shapes are becoming increasingly complex and often unconventional. Due to these characteristics, particular attention has to be paid to the robustness of these structures, which have to face a variety of environmental loads while still remaining cost effective. In particular, wind loading can play a fundamental role in the design process and has to be accurately assessed with respect to both structural integrity and serviceability (Irwin (2009); Blocken and Gualtieri (2012); Owen *et al.* (2013)). Turbulence is naturally present in the Atmospheric Boundary-Layer (ABL), together with aerodynamic phenomena typical of bluff bodies, such as vortex shedding and intermittent reattachment of shear layers, causes the structure to experience dynamic forces which lead to along-wind and across-wind vibrations. The traditional approach for the assessment of wind loads on slender structures strongly relies on boundary-layer wind tunnel practice.

For more than a century, the wind tunnel has been the preferred choice of determination for wind loading on buildings and structures. The procedure on how to conduct a study of wind loading on scale models in a wind tunnel facility has been iteratively refined in parallel to the increasing wisdom of wind characteristics itself, and how it manifests as loading on a structure or as its direct static of dynamic response. A milestone in this connection is the specifications by Jensen (1958) for using a turbulent boundary layer in wind loading studies, reflecting an ABL. Henceforth, the formulation of scaling laws, the exploration of their feasibility are at the focus of research and engineering application, and are frequently reviewed through comparison to full-scale (field) measurements, or cross-comparisons to other wind tunnel facilities on benchmark geometries or techniques (e.g. Holmes (2014)). The historical evolution of the wind tunnel technologies has been extensively covered by Cochran and Derickson (2011). The advances in measurement techniques, computational power and data acquisition capability contributed in its own right to the present state-of-the-art wind tunnel tests. However, even with today's wisdom of the subject, the fact remains that studies replicated at two or more wind tunnel facilities are likely to show a considerable scatter of measured data (Bruno. *et al.* (2014)). To ensure a certain degree of quality control for these experiments (and consequently of the results), guidelines for wind tunnel testing have been issued by a number of Wind Engineering organisations, e.g. American Society of Civil Engineers (ASCE); and Architecural Institute of Japan (AIJ).

Concurrently, over the last few decades, Computational Fluid Dynamics (CFD) has proved its value as an effective tool in wind-related studies, where the improvements in the scientific work have accelerated with the progress in computational capacities. Driven by the development within the aerospace and automotive industries, it has established itself as a standard tool for investigators of wind comfort in urban areas, for studies of building ventilation or fire safety simulation. As the credibility of CFD has accelerated in these fields, many larger civil engineering consultancies maintain a CFD department, which conduct a variety of tasks related to fluid dynamics and wind engineering. This practice has merited its own discipline of Computational Wind Engineering (CWE). In the literature, Cochran and Derickson (2011) and Blocken (2014) have reviewed a number of wind-related tasks that can be elucidated using CFD, and Cochran. *et al.* (2015) provided a discussion on which wind-related tasks should be conducted using CFD to enhance building design.

Unlike the wind tunnel, CFD draws its strength from being readily available for anyone with a computer, capable of considering field variables that are difficult to implement and control for experimental tasks (such as temperature), and faster execution on high-performance computers. In the context of wind loading, CFD modelling is capable of capturing fluctuating pressures over a model structure using a large number of passive sampling points stationed over its surface. In contrast, wind tunnel tests attain this information though the implementation of pressure taps - a technique that provides limited information of the flow (e.g. separation regions) and is impractical for structures with complex designs.

To simulate turbulent flows, CFD simulations based on the Reynolds-Averaged Navier-Stokes models have been extensively investigated over the past few decades. However, such models are often found to be inaccurate where wind loads on bluff bodies are concerned and their predictive capability is limited to mean flow properties, while the ability to accurately predict turbulent fluctuations is recognised to be of fundamental importance for the assessment of the dynamic response of structures (Huang *et al.* (2010)). The need to correctly take into account the flow dynamics has led researchers to move towards scale-resolving turbulence approaches, such as Large Eddy Simulation (LES). Although this technique is considered to be well suited for the analysis of flows around bluff bodies, it has often been observed that results from these are considerably scattered, even when simple geometries are considered (Bruno. *et al.* (2014); Patruno *et al.* (2016); Ricci *et al.* (2017)). Indeed, the complex, instability-driven phenomena observed in the turbulent flows around bluff bodies, such as shear layer detachment/reattachment and vortex shedding, render the simulation of this kind of flow an extremely challenging task, and results are often found to be dependent on the simulation setup and the adopted turbulence Sub-Grid Scale (SGS) model (Ricci *et al.* (2017)). Additionally, it should be noted that the generation of realistic unsteady boundary conditions, able to reproduce the main features of the turbulence found in the ABL, is imperative in order to obtain accurate results in terms of pressure distributions and, resulting forces acting on the structure. Among other structures, this fact has been observed for high-rise buildings and, in particular, in the framework of the CAARC benchmark (Melbourne (1980)), since results of different turbulent inflow generation techniques were analysed in this case (Daniels *et al.* (2013); Dagnew and Bitsuamlak (2013, 2014); Aboshosha *et al.* (2015); Yan and Li (2015); Elshaer *et al.* (2016)).

Although the advances of CFD techniques is encouraging, some extensive research and material are still imperative. The flow around an obstacle becomes extremely complex at high Reynolds numbers, and scattered results in both experimental and numerical results usually occur. Bruno. *et al.* (2014) conducted a large benchmark study of 70 experimental and numerical studies, where they found that the drag force can be estimated quite accurately with CFD, whereas the estimation of aerodynamic lift showed the greatest disparity in the results. This large scatter of CFD results was believed to be due to the choice of turbulence models, grid topology/resolution, sub-grid scale models etc. The study substantiates that extensive research is necessary for the wind loading determination with CFD, where the accuracy and reliability is clear in consequence of the settings, to ensure a certain quality of the tests, as for conventional wind tunnel tests. Likewise, the need for a CFD guideline for CWE is now in demand, to ensure future researches to follow the same restrictions and so that CFD wind loading simulations can attain the same status as for wind environment simulations.

The Japanese building authorities (AIJ) published the first CFD guideline for structural purpose in 2015, where they accept CFD simulations for wind loading studies, provided knowledgeable handling of the software and critical surveillance to be performed by an experienced wind engineer (AIJ (2017)). Unfortunately, the guideline is only published in Japanese, and the desire for an English translation is still present. Nevertheless, CFD is already a strong tool that can be utilised during the design cycle of a structure. CFD can be applied to reduce the time consumption and secure a faster response, since geometrical modifications easily can be carried out, and Computer-Aided Designs tools are incorporated directly with the simulation setup. It is therefore conceivable that CFD will be a larger part of the design phase in engineering consultant companies, and thereby complement wind tunnel tests. Instead of opposing the two methods, the strengths from each method should be adapted to combine into a hybrid approach. Thoughts on this to carry out more efficient projects are examined by Meroney (2016).

This contribution focuses on the application of LES towards the determination of the wind loading on slender structures, with an emphasis on status of freestream turbulence generation and the incurring aeroelastic responses. Effects of freestream turbulence

on the identified flow phenomena is also discussed. The current state and potential use of LES is examined. In particular, in order to independently estimate the accuracy or reproducibility of numerical results obtained by LES for wind-related phenomena, comparison with wind tunnel data is examined for a number of cases from different viewpoints. This paper particularly emphasises the importance of such a comparison, concludes with an evaluation of the turbulent inflow generation methods considered, and raises a discussion of important aspects of LES that need to be scrutinised in future studies.

The topic of this review is explored through a simplified geometry, i.e. of a rectangular cross-section. Tall buildings are often shaped as elongated prisms. Two-dimensional rectangular cylinders have commonly been considered as qualitative schematics of bridge sections (e.g. Matsumoto (1996); Ricciardelli *et al.* (2002); Bruno *et al.* (2010, 2012); Mannini *et al.* (2017)). For a cross-section with perfectly sharp corners and smooth surfaces, the side ratio alone defines the rectangular geometry, which, due to its simplicity, can provide a deep insights into important fluid dynamic phenomena, and allows a detailed study of the aerodynamic features of the incurring flowfield (e.g. Yazdi *et al.*, 2010). Moreover, depending on the side ratio, and turbulent characteristics of the freestream flow, rectangular cross-sections are prone to different types of flow-induced vibration.

This manuscript reviews more than 100 publications by various authors on the subject of wind loading on slender structures; of these, it should be noted that the specific topic of LES to assess wind loading is fairly new and is relatively limited on contributions at the time of writing. Consequently, a comprehensive discussion of this subject is out of scope of this paper. Nevertheless, this overview is timely, and can be considered a useful contribution to wind engineering.

2. The Atmospheric Boundary Layer

The challenge of simulating wind, whether it be through an experimental or numerical wind tunnel, is to build up a fully-developed turbulent boundary layer, of which the mean velocity and turbulence intensity profiles, correlation functions and power spectra reflect the characteristics of the ABL. In the following, the fundamental parameters used to measure the degree of a fully-developed ABL, in both an experimental and numerical wind tunnel, is described.

The mean wind velocity profile in the streamwise direction is described either by a *logarithmic* or *power* law. Typically, when considering high-rise buildings, the power-law is applied:

$$u(y) = u_{ref}\left(\frac{y}{y_{ref}}\right)^{\alpha}. \tag{1}$$

The subscript ref denotes a reference value known *a-priori*, i.e. a reference velocity u_{ref} must be known at height y_{ref} . The parameter α is dependent upon the terrain roughness and the stability of the ABL. The power-law model shows good agreement with the upper region of the ABL, but fails to accurately capture the profile for the lower regions (see Huang *et al.* (2007)).

When considering the velocity $u(t)$, the mean and variance of the signal can be described:

$$\langle u\rangle = \lim_{T\to\infty}\frac{1}{T}\int_0^T u\ dt, \tag{2}$$

and

$$\sigma_u^2 = \langle u'^2\rangle = \lim_{T\to\infty}\frac{1}{T}\int_0^T (u-\langle u\rangle)^2 dt. \tag{3}$$

where $\langle\rangle$ indicates the time-averaged value. σ is the standard deviation, referred to as root-mean-squared (rms) of the velocity fluctuations. The magnitude of fluctuation can be characterised by the *turbulence intensity*:

$$I_u = \frac{\sigma_u}{\langle u\rangle}. \tag{4}$$

Since wind in the ABL is anisotropic, the turbulence intensity is expressed for the lateral (w) and vertical (v) directions with a relation to the mean wind velocity in the streamwise direction.

$$I_v = \frac{\sigma_v}{\langle u\rangle}; \qquad I_w = \frac{\sigma_w}{\langle u\rangle}. \tag{5}$$

Turbulent flow is also characterised through convolutions, cross-correlations, and autocorrelations, which are used to identify repeated patterns in the field variable signal or signals. Of these, The autocovariance and autocorrelation measure the directional relationship of a signal. For the fluctuating velocity signal, these are are respectively defined:

$$r(\tau) = \langle u'(t)u'(t+\tau)\rangle, \tag{6}$$

and

$$R(\tau) = \frac{r(\tau)}{\sigma_u^2}, \tag{7}$$

where τ is the lag. The autocorrelation coefficient R may take the range $0 \le R \le 1$ where $R \to 0$ indicates uncorrelated signals, and $R \to 1$ perfectly correlated signals. These definitions are used to estimate the turbulence integral time and length scales. The integral time scale may be obtained from an autocorrelation coefficient in time as

$$T_u = \int_0^\infty R(\tau)d\tau. \tag{8}$$

One option is to integrate the above autocorrelation function from $\tau = 0$ to where the autocorrelation coefficient first reaches zero. It should be noted that after this point the function can revolve around zero, producing a positive and negative value, or it may never reach a zero. In the latter situation, other options have to be considered.

Since it is generally more convenient to sample data in time rather than space, Taylor's frozen turbulence hypothesis (Taylor, 1938) may be used to estimate the integral length scale. This requires that $u' << \langle u \rangle$, which is true for homogeneous isotropic turbulence but may not be valid in shear flows (Pope (2000)). Assuming that Taylor's hypothesis holds, the integral length scale can be defined

$$L_u = \langle u \rangle T_u. \tag{9}$$

The integral length scale can be interpreted as the mean diameter of the largest eddy in the freestream flow. The turbulence process in natural wind is further characterised in terms of the Power Spectral Density (PSD), describing the energy distribution between the large and small scales of motion. The PSD can be determined through a Fourier transform of Eq.6:

$$S_u(\omega) = \frac{1}{2\pi} \int_{-\infty}^{+\infty} r(\tau) \exp(-i\omega\tau) d\tau, \tag{10}$$

where the angular frequency $\omega = 2\pi f$. The PSD for wind engineering applications has been expressed in a number of mathematical forms. The most widely used being the von Kármán spectrum for the flow direction, and the modified spectra for the lateral and vertical directions, which are described:

$$S_u(f) = \frac{4\sigma_u^2 \frac{L_u}{\langle u \rangle}}{\left[1 + 70.8 \left(\frac{f L_u}{\langle u \rangle}\right)^2\right]^{5/6}}; \tag{11}$$

$$S_i(f) = \frac{4\sigma_i^2 \frac{L_i}{\langle u \rangle} \left(1 + 188.4 \left(\frac{2 f L_i}{\langle u \rangle}\right)^2\right)}{\left[1 + 70.8 \left(\frac{f L_i}{\langle u \rangle}\right)\right]^{11/6}}, \tag{12}$$

where $i = v$ or w.

3. Turbulence modelling approaches

The choice of a sufficient turbulence model for generating wind loads is of high importance and it is crucial to perform a time-dependent simulation to simulate stochastic time processes. Therefore, the Reynolds-Averaged Navier-Strokes (RANS) turbulence model is not considered, since a steady-state is sought as a solution and thus only 'average' loads are computed. Consequently, both RANS and Unsteady-RANS (URANS) models are incapable of resolving the flow field around a building, specifically the recirculation of vortices at the wake and the separation zones (Blocken (2014)). This was also substantiated by Huang *et al.* (2007), where both the pressure and suction zones were over-estimated with different RANS models.

The accuracy of turbulence simulation is dependent on the choice of turbulence model and the grid resolution. Fig.1 illustrates the PSD of turbulent flow, and the philosophy of the most notable modelling approaches. The Kolmogorov -5/3 power law is also marked in the figure and is of high importance, as it identifies the inertial subrange

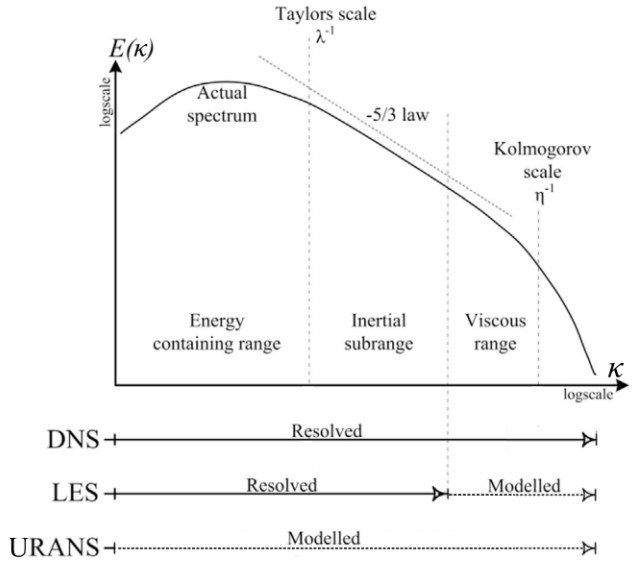

Figure 1. Power Spectral Density (energy cascade) and philosophy of turbulence model approaches .

- a critical region establishing the breakdown of eddies (vortices) in the flow into 'large' and 'subgrid' scale (SGS) eddies in LES.

Direct Numerical Simulation (DNS) is considered the most accurate approach of simulating turbulent flow, where all scales of motions down to the Kolmogorov length scale are resolved, i.e. a full time-dependent solution of the continuity and Navier-Strokes equations is sought. Since DNS resolves the smallest eddies, the method demands both an exceptionally fine mesh and consequently extensive computational resources. Moreover, the proportional relationship between Reynolds number of the flow and disparity between the largest and smallest scales of motion restricts the application of DNS to a limited number of cases, such as at relatively low Reynolds number and with a simple geometry. Due to the high Reynolds numbers observed in natural wind, DNS is computationally infeasible for the immediate future.

LES also directly addresses the turbulence processes, but in contrast to DNS, only the large-scales are resolved, and the unresolved small-scale fluid motions are modelled through a SGS model. The LES method averages Navier-Strokes equations over a small volume (e.g. grid) in space, meaning that a filter operation is introduced, where eddies larger than the filter-length (typically the grid size) are resolved, and eddies smaller than this are modelled. This 'cut-off' between the resolved and modelled eddies is often positioned at the upper limit of the inertial subrange, where the length-scale is much larger than the Kolmogorov length-scale (see Fig.1), thus enabling the use of a larger time-step and grid resolution (than DNS) for simulations at higher Reynolds numbers. Tamura *et al.* (2008) stated that the grid resolution should be

large enough to capture the inertial subrange for the streamwise velocity component. Moreover, Jø rgensen *et al.* (2014) showed that resolving more than 80% of the turbulent kinetic energy (TKE) would be sufficient to capture the important physical processes of the flow, ensuring that the simulation is well-resolved and is capable of capturing the real trends of the wind flow around the target structure.

The formulation of a physically realistic SGS model requires understanding of the physics and the statistics of scale interactions in turbulence, and is therefore an open research question owing to the fact that turbulence remains an unsolved problem in classical physics. The Smagorinsky model (Smagorinsky (1963)) is considered as the pioneer SGS model for LES, and is noted for its simplicity and computational cheapness. However, the models suffers major drawbacks for its purely dissipative nature and inability to account for backscatter (inverse energy cascade). This model is also unable to capture the dampening of eddies in near-wall regions, and therefore requires ad-hoc modifications to fulfil this behaviour, such as that suggested by van Driest (van Driest (1956)). Later, Dynamic SGS models based on the Smagorinsky model were proposed (e.g. Germano *et al.* (1991)) which endeavour to improve the solutions for wall-bounded flows, at a significant increase in computational expense. More recently, Nicoud and Ducros (1999) proposed the Wall-Adapting Local Eddy-viscosity model to overcome the shortcomings of LES for near-wall flows, without a dynamic procedure, making it less computationally expensive. These models have been implemented in most commercial CFD software and are often adopted in wind loading simulations.

To summarise, at present it is advised to use the LES approach when using CFD to determine wind loads assuming the computational cost is affordable for the CFD user, since it requires less computational capacity than the DNS method and is more accurate and reliable than URANS. Nevertheless, within the CFD community, several topics need to be satisfactorily addressed for LES in order to advance its use in industry, including:

1. Generation of inflow or initial turbulence by numerical or statistical methods;
2. Sophisticated and accurate SGS turbulence modelling for unsteady separated flows or turbulent boundary layers over rough surfaces;
3. Numerical discretisation with conservation of various physical quantities for modelling complicated geometries or moving walls;
4. Near-wall modelling or treatment for high Reynolds number flows.

This review addresses the first of these topics, as its advancement is critical for an effective application of LES to wind loading assessment.

4. Review of inflow generation methods for LES

For a wind engineering application, the generation of inflow turbulence, which provides time-sequential data with physically corrected spatial structures, is particularly important to simulate natural wind. A comprehensive review of inflow techniques for LES is beyond of the scope of this article, and the authors refer the reader to see to Tabor and Baba-Ahmadi (2010); Bercin *et al.* (2018) on this topic. For the sake of brevity, a handful of methods applied in the field of wind engineering are outlined here. These methods can be categorised into four main groups, which are illustrated in Fig.2.

4.1. Wind Tunnel Replication

A somewhat intuitive method to generate the upstream turbulent flow in a numerical wind tunnel is to construct an exact replica of the target experimental setup, introducing spires and roughness elements into the domain, as illustrated in Fig.2(a). In this way, a turbulent boundary layer is generated in the same manner as the conventional wind tunnel experiments. Because of this, a good agreement between experimental and numerical results is attained (in theory). However, the shortcoming of this method is that a local fine mesh is required along the upstream to generate a fully developed boundary layer over the target model, resulting in an extremely expensive simulation.

The method was applied by Phuc *et al.* (2014), who achieved good agreements between the experimental wind tunnel results and the numerical Wind Tunnel Replication results. They conducted simulations of three different grid resolutions, where it was observed that the correlation between the experimental and numerical results were significantly improved using a refined mesh. Similar results and conclusions was found by Capra *et al.* (2018). The method was also examined by Jø rgensen *et al.* (2014), who suggested that it is necessary to ensure a PSD generated in a numerical simulation to reflect an experimental wind tunnel.

4.2. Precursor Database

The Precursor Database method is fundamentally identical to the above method, but instead of simulating a full wind tunnel, the test section is omitted and the upstream wind flow time series data is recorded on a 2D plane and saved in a database. This is called the precursor domain as seen in Fig.2(b), where the saved 2D database is illustrated as the purple 2D plane. Subsequently the simulation of the test section domain can be executed, where the stored 2D plane transient data is used as the inflow boundary conditions of the simulation. This method also requires a large amount of computational power, but in contradistinction to the Wind Tunnel Replication method, the stored 2D plane database can be reused for further wind simulation studies. Likewise, it is relatively simple to obtain a good match between experimental and numerical results.

In its application for wind loading simulations, this method is widely used in Asia (e.g. Yoshikawa and Tamura (2012, 2013)),

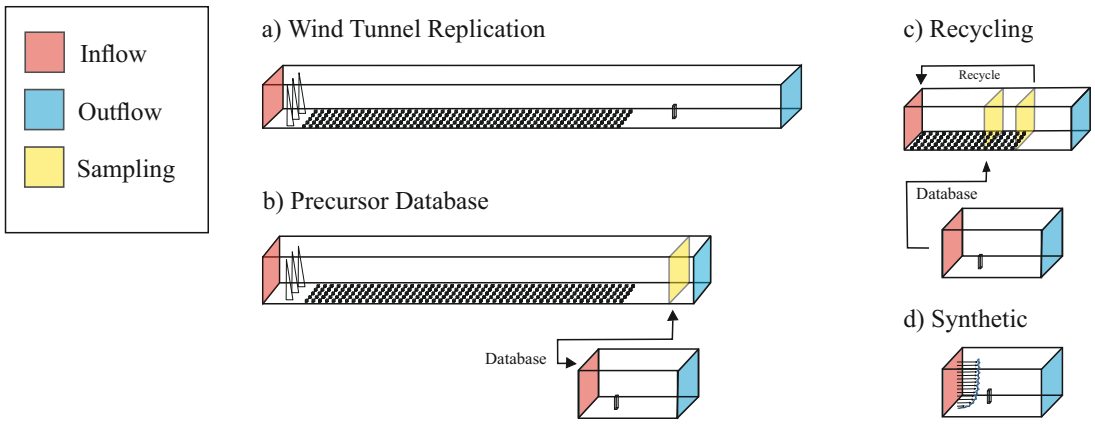

Figure 2. Schematics indicating the four main groups of inflow generation methods for LES. Redrawn (and expanded on) from Dagnew and Bitsuamlak (2013, 2014); Thordal *et al.* (2019).

where the studies showed promising agreements between the experimental wind tunnel results and the LES data. Concurrently, this method has been successfully applied for wind farm simulations Stevens *et al.* (2014); Breton *et al.* (2017).

4.3. Recycling Method

Like the Precursor Database method, the Recycling Method also consists of an auxiliary domain and a test section domain. However, contrary to the Precursor Database, the auxiliary domain in this method recycles the flow until the boundary layer is statistically stable and reflects the parameters of the turbulent boundary layer, where the fundamental idea is to reuse the solution downstream of the driver domain as the inlet boundary condition. This is carried out by recycling the flow near the outlet boundary of the driver domain, reintroducing it at the inlet boundary and subsequently mapping it into a data file in a vertical 2D plane when the flow is stable. This is illustrated in Fig.2(c), where the first purple plane is the mapped flow that subsequently is used as the inlet boundary conditions in the test section domain.

The method was proposed by Lund *et al.* (1998) for a smooth wall. Since a boundary layer is spatially developed over the wall, the flow at the outlet is rescaled to match the inlet boundary. In this approach, the flow is decomposed into the mean flow and fluctuating flow and treated differently before it is recycled. The flow is rescaled to satisfy the law of the wall in the inner region and the defect law in the outer region of the boundary layer, whereupon a weighted average of the flow in the entire boundary layer is formed by means of a weighting function.

Kataoka and Mizuno (2002) simplified the Recycling Method by assuming the boundary layer thickness is constant in the driver domain. This is implemented by introducing a damping function, which ensures the boundary layer will not spatially develop and hence the rescaling procedure is omitted. The simplified approach then only reintroduces the fluctuating flow at the outlet boundary to the inflow boundary in the driver domain, since the mean flow is not changed throughout the driver domain.

Lund et al.'s method was also further extended by Nozawa and Tamura (2002) for a rough wall. The approach is principally unaltered, where the flow is decomposed into a mean and a fluctuating flow and treated differently. The mean flow is similarly rescaled and recycled, whereas the fluctuating flow instead is addressed with a scaling parameter for a rough wall.

As seen in Fig.2(c), the auxiliary domain can get reduced to half the size or less than the Precursor Database method, which implies that the grid size is significantly decreased and thereby also the numerical solver time is reduced. Furthermore, the fetch where the turbulent flow is built up can be simulated as being infinitely long, which is an advantage compared to the Wind Tunnel Replica Method and Precursor Method.

The Recycling Method is widely used in wind engineering, especially for comparison studies between different inflow generation methods, as composed by Dagnew and Bitsuamlak (2014) and Yan and Li (2015). Nozu *et al.* (2015) utilised the method for a study of an urban city, where they showed encouraging comparisons between numerical and experimental results.

4.4. Synthetic turbulent generation

All the above methodologies set the inflow conditions from a 'real' generation of turbulence. It is therefore expected for the resulting turbulent field to possess the required crucial statistical characteristics, including temporal and spatial correlations and PSD. However, the fundamental drawback of these methods is that the turbulence statistics of the generated inflow turbulence

complies with the predefined settings of the driver domain, such as the domain size and the rough wall. Another drawback is the additional expensive computational cost for the generation of the inflow turbulence. These make those methods impractical for use in industry.

An alternate method is to synthesise the turbulence at the inflow plane without a precursor simulation, as illustrated in Fig.2(d). In this approach, a pseudo-random coherent field of fluctuating velocities, with spatial and time scales, is superimposed on a predefined mean profile. Potentially this makes the domain significantly smaller than the methods listed above, entailing a faster solution time at a lower computational costs. With its appealing aspect of being relatively inexpensive, several synthetic turbulent generation methods have been proposed in the literature. The velocity perturbations can be generated through several different ways, such as spectral-synthesising (with its variants), digital-filter based, and Proper-Orthogonal-Decomposition (Tabor and Baba-Ahmadi (2010)).

This subject is extensively discussed in the following subsections on several widely used synthetic turbulence generator methods used in wind engineering. Examples of other synthetic methods include the Forward Stepwise Method (e.g. Bercin *et al.*, 2018), and the hybrid approach of Xie and Castro (2008b) and the Wind Tunnel Replication Method, (e.g. Wingstedt *et al.*, 2017a,b).

4.4.1. Random Flow Generation (RFG)

The family of synthetic methods can be divided in several groups (see Bercin *et al.* (2018)). One such group consists of spectral methods, in which turbulence is generated through a superposition of harmonic functions with random coefficients. The Random Flow Generation (RFG) method by Smirnov *et al.* (2001), developed on the work of Kraichnan (1970), falls in this category. The method can generate an isotropic divergence-free fluctuating velocity field satisfying the Gaussian's spectral model as well as an inhomogeneous and anisotropic turbulence flow, provided that an anisotropic velocity correlation tensor is specified. The method is readily available in commercial CFD software.

4.4.2. Discretising and synthesizing Random Flow Generation (DSRFG)

Due to its generated spectrum in a Gaussian form, the RFG method is seriously limited in cases where the energy content of the inertial subrange cannot be discarded for high Reynolds number flows. Hence, Huang *et al.* (2010) modified the RFG method to satisfy any arbitrary model spectrum. This property is especially appealing for wind engineering applications, where the von Kármán model is widely adopted. A remarkable feature of this method is its highly parallelisable implementation, since the generation of the fluctuating velocity series is independent for each node at the inflow plane. However, this also implies that the computational cost to generate the inflow turbulence data is proportional to the resolution of the inflow, which, in the context of LES, could be expensive. As their methodology introduces discretising and synthesising procedures to generate the inflow turbulence, the authors named this approach the Discretising and Synthesizing Random Flow Generation (DSRFG) method.

The DSRFG method has largely been used in recent comparison studies, such as Dagnew and Bitsuamlak (2014); Yan and Li (2015); Zhang *et al.* (2015) for the flow around a tall model building. These authors also outline the limitations of this method, and thus it was further extended. The most recent well-developed techniques are explained in the following subsections 4.4.3-4, together with the insufficiencies and limitations that were grounds for the new methods.

4.4.3. Modified Discretising and synthesizing Random Flow Generation (MDSRFG)

Castro *et al.* (2011) were critical of the DSRFG method, due to the insufficient inputs for time scales and statistical characteristics of the turbulent flow field. They subsequently introduced modifications to maintain the statistical characteristics in the flow, renaming this the Modified Discretising and Synthesising Random Flow Generation method (MDSRFG). Like the DSRFG method, the computational cost to generate the inflow data is proportional with the grid resolution at the inflow plane, as well as the number of specified Fourier modes considered.

4.4.4. Consistent Discrete Random Flow Generation (CDRFG)

Aboshosha *et al.* (2015) made further modifications to the DSRFG approach to capture the target spectral model. They also made modification to take the correlation function into account, so that the turbulent length scales are consistent in the flow field. They denoted their modification the Consistent Discrete Random Flow Generation method (CDRFG). Their work showed encouraging agreements between wind tunnel tests and LES. The code to develop the synthetically generated inflow boundary condition is enclosed in the appendix of their paper. Again, like the DSRFG method, the computational cost is proportional to the grid resolution of the inflow and number of Fourier modes considered, forcing the original authors to conduct their study on a very coarse computational grid.

4.4.5. Digital-Filtering

Another relevant group of synthetic inflow generators are those using digital filtering methods, whose aim is to generate velocity perturbations through randomly generated data (containing zero-mean and unit-variance) with a filter based on a correlation function (for instance, Gaussian or exponential). The correlations are therefore imposed directly, not through a prescribed energy spectrum. From the point of view of feasibility, the attractive feature of the digital-filtering method is its ability to impose a two-point spatial correlation directly rather than indirectly through an energy

spectrum as in the RFGs described above (Wu (2017)). Some early examples of digital filter methods include those by Klein *et al.* (2003); di Mare *et al.* (2006). Xie and Castro (2008a) expanded on the work of Klein *et al.* (2003) to improve the spacial and temporal correlations across the inflow plane, applying this to an array of wall-mounted obstacles with encouraging results.

A fundamental drawback of the digital-filtering method is the generated turbulent field cannot satisfy the continuity condition (divergence-free), creating artificial fluctuations in the pressure field. A plausible solution to this was proposed by Kim *et al.* (2013). The resulting 'XCDF' approach (named after Xie and Castro with the addition of a Divergence-Free methodology by Kim et al.) has the important property of satisfying the divergence-free requirement at minimal cost. This method has successfully been employed to study the flow around a tall model building (Daniels *et al.* (2013)) and an airfoil (Kim and Xie (2016)). More recently, starting from the work of Xie and Castro (2008a), Okaze and Mochida (2017) further expanded on the method using Cholesky decomposition of the turbulence-flux tensors and scalar fields (e.g. temperature, contaminant concentration), with prescribed temporal and spatial correlations. The performance of the above methods have been investigated in detail by Bercin *et al.* (2018).

4.4.6. Vortex method

An approach by Sergent, explained by Mathey *et al.* (2006), belongs to the third category of the synthetic turbulence generation methods, in which a random 2D vortex method is applied at the inflow plane to add perturbations on a specified mean velocity profile. This method can generate a velocity field that is both temporally and spatially correlated, provided that reasonable profiles for the mean turbulence kinetic energy and dissipation rate are provided. However, different from the methods discussed above, the target spectrum and statistical characteristics for the inflow turbulence as well as inhomogeneity and anisotropy of turbulence are not explicitly expressed in its generating procedure.

This method is incorporated in commercial software, where the user needs to specify the number of vortices over the inflow boundary (typically $N/4$, where N is the number of nodes over the inflow boundary).

4.5. Feasibility of the inflow generation methods

The advantages and disadvantages of the above methodologies are judged through their ability to generate the turbulent statistics (i.e. spatial correlations, turbulence intensities etc.) to correspond with the prescribed target characteristics, and the required computational cost. For the Replication and Precursor approaches, the required grid resolution and incurring computational cost make them infeasible for an effective use in industry. At the same time, the resulting turbulent statistics, while in theory would be a replica of the target wind tunnel, are still limited by the numerical diffusion associated with the SGS modelling for LES. An effective use of these methods would therefore require an exceptionally fine grid.

Regarding the synthetic inflow methodologies, a topic that has not been addressed in the literature is the relation of input parameters for each approach and the physical attributes they represent to generate the turbulent flowfield. The RFG and DSRFG methods require the user to prescribe profiles for the mean velocity profile, length scale (magnitude), and cross-correlation tensor to generate anisotropic turbulence. The modified versions of these, and digital-filter methods, require the user to prescribe more correlation tensors along with the turbulent length and time scales. These can be roughly estimated through an initial RANS calculation, or simplified semi-empirical approximations (e.g. Stull (1988); Billson *et al.* (2004)). However, for direct comparison, it is best to fine-tune these parameters using data from the target wind tunnel (Dagnew and Bitsuamlak (2014); Yan and Li (2015)). This however provides a fundamental problem for validation studies. Not all the required turbulent statistics for the inflow methodology are recorded in wind tunnel reports, either for lack of foresight, or due to a limited ability to attain such data.

To successfully run LES, one would require wind tunnel studies to supply the necessary input data for synthetic inflow conditions. Alternatively, optimisation methods could be utilised to determine to missing information based on target pressure data (Lamberti *et al.* (2018)). Traditionally, validation studies have been conducted using mean wind velocity and turbulence intensity profiles supplied by the target wind tunnel. These are quite straightforward to replicate, there are however other characteristics of the turbulent flow that need to be satisfied.

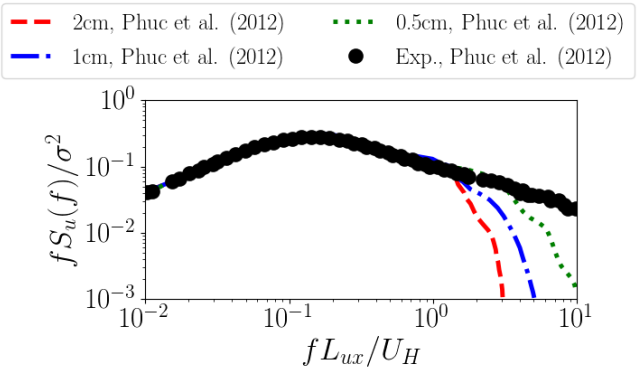

Figure 3. Comparison of PDS for the streamwise direction between the von Kármán spectrum, an experimental wind tunnel test and a numerical simulation generated with an exact replica of a wind tunnel with three different grid resolutions (cell sizes). Redrawn from Phuc *et al.* (2012)).

The PSD of the ABL follows the von Kármán model (Eq.11). Phuc *et al.* (2012) compared the von Kármán spectrum model, an experimental wind tunnel test, and a LES of an exact replica of the wind tunnel setup with three different grid resolutions. The resulting spectra are shown in Fig.3. It can be seen in this figure that the energy generated in the lower frequencies is clearly replicated using LES, and more of the spectra is captured along the intertial subrange with increasing grid resolution (reducing grid size). The resulting number of cells for the simulation is extremely large (expensive), even for typical LES studies. Similar results were produced with the Precursor Database Method by Yoshikawa and Tamura (2012) as illustrated in Fig.4. Likewise, excessive diffusion can be seen in the simulation for non-dimensional frequencies (fL_i/U) above 1, indicating that the transition between resolved and modelled turbulence is located in this region.

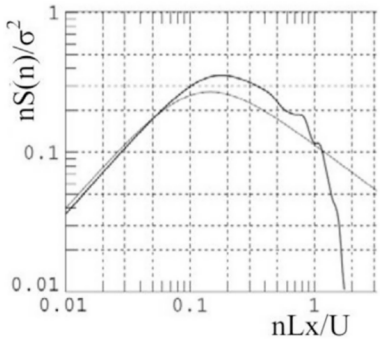

Figure 4. Numerically generated PSD for the streamwise direction with the Precursor Database Method compared with the von Kármán spectrum (Yoshikawa and Tamura (2012)).

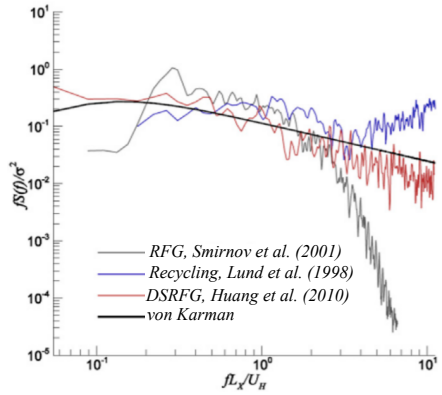

Figure 5. Comparison of PSD for the streamwise direction between the von Kármán spectrum at the model and various inflow methods at building height. (Dagnew and Bitsuamlak (2014)).

Dagnew and Bitsuamlak (2014) compared the spectrum of three inflow conditions in Fig.5; this includes the original RFG method by Smirnov *et al.* (2001), the DSRFG method by Huang *et al.* (2010) and the Recycling Method by Lund *et al.* (1998). As expected, the PSD is poorly captured for the original RFG method, since it does not satisfy the von Kármán model, while the Recycling Method produces excessive *backscatter*, and hence the energy dissipation does not reflect a realistic wind flow. The DSRFG method by Huang *et al.* (2010) showed a smallest discrepancy with the von Kármán model for the higher frequencies. Similar trends for the RFG method can be seen in the spectra by Yan and Li (2015) in Fig.6. The Recycling Method however follows the von Kármán model very well for the lower frequencies, but is too diffusive for non-dimensional frequencies above 1. Similar to the results from Dagnew and Bitsuamlak (2014) study, the best match to the von Kármán model is generated with the DSRFG method by Huang *et al.* (2010). It should be noted that the digital-filtering XCDF method by Kim *et al.* (2013) is also able to match the von Kármán model, as seen in Fig.7, at a cheaper cost to the DSRFG method.

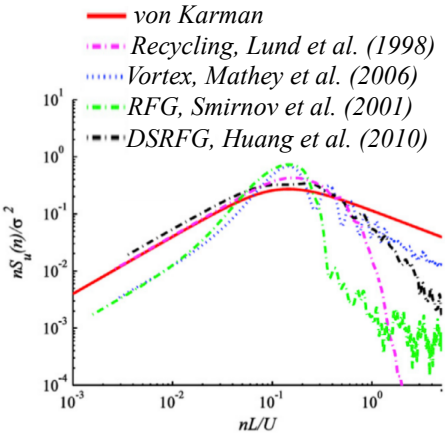

Figure 6. Comparison of PSD for the streamwise direction between the von Kármán model and various inflow methodologie. Original source: Yan and Li (2015).

The above studies claim the discrepancies between the von Kármán model and the PSD for the higher frequencies is due to the local grid size, resulting in a larger contribution of the SGS model. The entire spectrum can only be captured through a DNS approach, entailing that excessive diffusion for the higher frequencies is almost unavoidable when applying LES. In order to represent a realistic wind field, Dagnew and Bitsuamlak (2014) suggest that the spectrum should fit the von Kármán model up to a non-dimensional frequency of 10, so that the inertial subrange is adequately resolved. This criterion refers to the sufficient representation of small-scale eddies (vortices) in the approaching wind compared to building model dimension, commonly associated to the occurrence of high local suction peak loading on the building envelope.

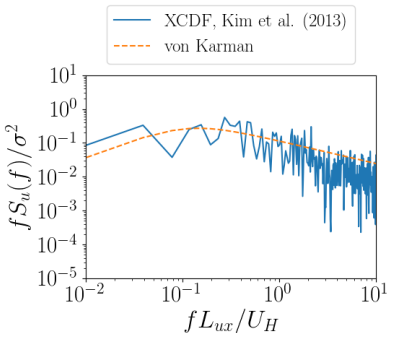

Figure 7. Comparison of PSD for the streamwise direction between the von Kármán model and a digital-filtering method (Kim *et al.* (2013)). Data from Daniels *et al.* (2013).

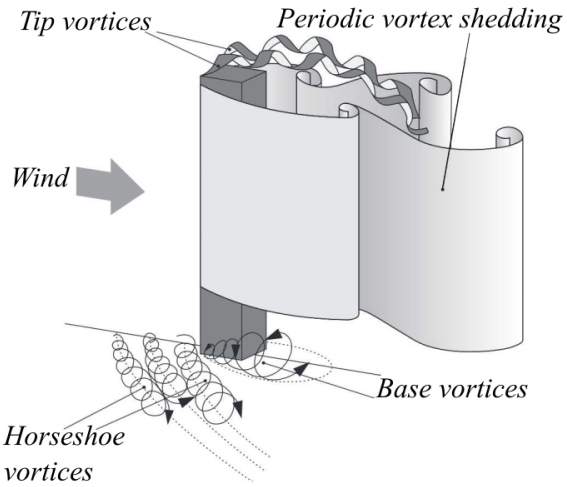

Figure 8. Identified flow structures around a wall-mounted square prism. Diagram source: Wang *et al.* (2004).

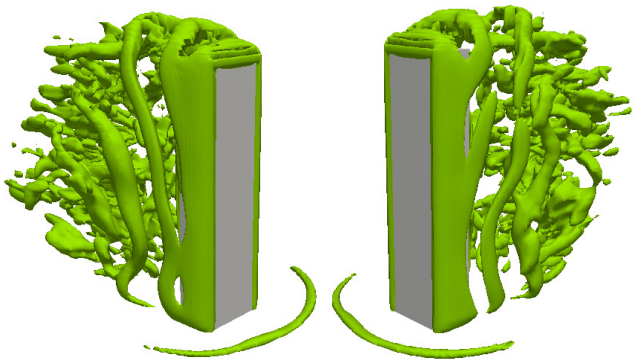

Figure 9. Iso-surfaces of the Q-criterion for the flow over the CAARC tall model building. Diagram source: Daniels (2016).

Melbourne (1979) argued that the deficit of small-scale turbulence in a simulated ABL is responsible for a significant difference of surface peak pressure between wind tunnel and full-scale data. Tieleman (1993) introduced a minimum threshold for small-scale turbulence, as approximately $1/10$ of the characteristic building dimension. As the synthetic inflow turbulence generation along with the LES techniques has the potential to generate more realistic inflow turbulence for high Reynolds number flows than that of the simulated ABL in a wind tunnel, there is a hope that the CFD can produce more accurate prediction of surface peak pressure.

5. Wind loading on an isolated tall building

Isolated high-rise buildings are inherently classed as slender due to their small width/depth ratio. For structures with a ratio less than 2 (e.g. Bruno. *et al.*, 2014; Chen *et al.*, 2019), the flow separation at the leading corners will not reattached along the building surface, and thus is engulfed in its own body-induced turbulence.

The properties of the turbulent freestream have a significant contribution to the distribution and magnitude of the wind load acting on the building. The largest loading is located the windward face of the building, and becomes less pronounced for the remaining sides. However, the formation of separation bubbles at the corners of the lateral sides causes extreme suction regions depending on the level of body-induced turbulence. The interaction of freestream to body-induced turbulence makes the relation between flow properties and resulting load characteristics difficult to determine.

Studies for the flow around a rectangular (or square) prism are typically treated as an analogy for the flow around high-rise buildings. Despite its simplistic geometry, the flow physics are still considerably complicated as the geometry contains both wall-mounted and open ends.These 'end-effects' encourage the flow to have a more three-dimensional characteristic; for example, towards the ground, the flow is subjected to intense mixing due to the interaction with the floor; on the opposing end, the flow circulates around the top and impinges on the wake. Between these two ends, the flow around the mid-height can be considered homogeneous (2D) along the vertical direction. Overall, it can be argued that the interest in studying the flow around a wall-mounted prism is two-fold: firstly, the prism represents a schematic of a tall building whereby the wind loading on the design provides very useful case study for industry; secondly, from a more academic point of view, the interaction of the flows between the prism end and the homogeneous region yields a wide range of coherent and complex structures which characterise bluff body flow (body-induced turbulence). Fig.8 summarises the identified flow structures around a tall model building (square prism); for comparison, Fig.9 shows the iso-surface plots of the turbulent structures obtained using LES.

The key characteristics of the wind loading on a tall building are now summarised. The windward wall is defined as the surface of the building to which the wind direction is normal. By Bernoulli's principle, a stagnation point is located on this face, and can be found approximately two-thirds of the building height, depending on the aspect ratio of the wall and the pitch of the roof (Bi (2006)). Above the stagnation point, the flow is drawn over the roof of the building and into the wake, creating a significant mixing of the flow. The literature also proposes that for certain cases, 'tip vortices' are formed at the leading edge of the roof, as illustrated in Fig.8. Below the stagnation point, along the centreline of the windward wall, a downsweep of the flow is created; it is speculated that increasing the height of the building increases the acceleration of this flow (Wang and Zhou (2009)). Towards the bottom of the building, this flow rolls up into a vortex, denoted as the horseshoe vortex, and convects around the lateral sides. This vortex induces a high shear region around the windward wall and has a significant effect on the distribution of pressures (Martinuzzi and Havel (2000)), while only having a weak influence on the wake (Sau *et al.* (2003)). The mean pressures on windward walls are positive (acting on the model) with a peak pressure value at the stagnation point. The formation of vortices at the windward edges creates a high suction pressure. At present, to the best of the authors' knowledge, quantification of these peak pressures at the immediate leading edge has not been performed in the literature. The leading edge vortices subsequently convect along the lateral sides of the building and into the wake, as demonstrated in Figs.8 and 9.

5.1. Surface pressures on a tall model building

A typical benchmark study of a single high-rise building is the Commonwealth Advisory Aeronautical Research Council building, also known as the CAARC building. The building is $183m$ high with a depth/width ratio of $2/3$ and a depth/height ratio of $1/6$. The CAARC building was proposed in the 1970s with the motive to calibrate wind tunnel measuring techniques. Melbourne (1980) summarised the pressure and force-balance data from 8 institutions with a significant disparity of results. Subsequent publications (e.g. Goliger and Milford (1988)) attributed this to the inconsistent inflow conditions.

Together with the rising interest of CFD, several numerical studies of the CAARC building are found in the literature with an emphasis on validating proposed modelling techniques. Most notable, Huang *et al.* (2007) provided a landmark paper comparing 8 numerical studies (4 RANS 4 LES with the RFG method (Smirnov *et al.* (2001)) to generate the inflow turbulence). Some important observations were made, such as the significant contribution of the mean velocity profile on the resulting mean wind loading (pressure). They also observed that the inconsistent distributions of turbulence intensity will have a significant impact on the fluctuating pressure (peak loading) on the lateral sides. It is therefore crucial to generate a freestream flow whose turbulent characteristic mimics the equivalent experimental study as closely as possible. This is crucial for the pursuit of understanding the flow physics around the geometry. With this in mind, this review will conduct a direct comparison for a number of inflow generation methods (see §4) to the equivalent wind tunnel case.

Two inflow cases are considered for this analysis. The target wind tunnel data of Dagnew and Bitsuamlak (2009) is chosen for the first scenario, where the turbulent inflow replicates *"Open grassland without trees"* (Davenport (1960)). The mean velocity profile was modelled using a wind power law exponent, α, of 0.12 (see Eq.1), with the turbulence intensity at the height of the building being $I_u = 14\%$. The other scenario is a *"Level country uniformly covered in scrub oak and pine"* (Davenport (1960)) through the target wind tunnel data of Huang *et al.* (2005), using $\alpha = 0.3$ and $I_u = 16\%$. The inflow conditions collected for comparison herein aim to mimic the turbulent statistics (length/time scales and intensities) of the target wind tunnel experiment.

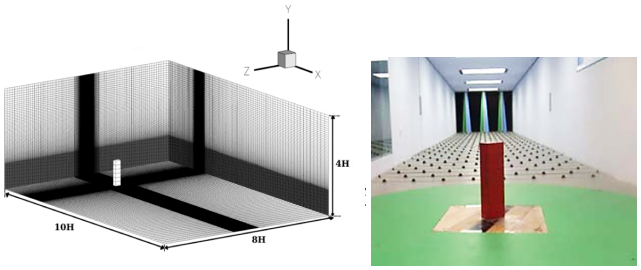

(a) CFD domain setup for LES in Daniels *et al.* (2013); Daniels (2016). (b) Boundary-Layer Wind-Tunnel configuration. Photo source: Dagnew and Bitsuamlak (2009).

Figure 10. Equivalent CFD and wind tunnel setups for the analysis of wind loading on the CAARC tall building model.

The mean surface pressure around the building model is defined

$$C_p = \frac{(\langle p \rangle - \langle p_{ref} \rangle)}{0.5\rho U_H^2}, \quad (13)$$

where p_{ref} is a reference pressure from the freestream, and ρ is the density of fluid, and U_H is the mean velocity of the incoming flow at the height of the model building. Similarly, the fluctuating pressure is defined

$$C_{p'r.m.s.} = \frac{p'_{r.m.s.}}{0.5\rho U_H^2}. \quad (14)$$

Fig.10 shows the equivalent LES and wind tunnel setup. Figs.11 and 12 show the surface pressure statistics around the perimeter at $2/3$ of the building height level for the two turbulent inflow scenarios. It can generally be seen in these figures that the mean pressure along the windward face are suitably replicated regardless of the inflow, since only a negligible deviation between the studies are seen. On the other hand, for the lateral and leeward faces, the discrepancies to the wind tunnel measurements are noticeable.

Fig.11 shows the results for the first inflow scenario. The wind tunnel measurements by Dagnew and Bitsuamlak (2009) are plotted alongside the numerical results of Dagnew and Bitsuamlak (2010, 2014); Daniels *et al.* (2013) using a wide range inflow generation methodologies. It can be seen that despite using the same inflow generation technique by Smirnov *et al.* (2001) (RFG), a significant disparity of mean surface pressures are seen between Dagnew and Bitsuamlak (2010, 2014). This is likely due to the coarser grid used in the earlier study. The discrepancies between the results of Dagnew and Bitsuamlak (2014) can be attributed to the inflow generation methodology. Unsurprisingly, the RFG inflow results show the largest difference with the validation data, despite calibrating the input data with the target wind tunnel experiment. As described earlier, this can be attributed to its inability to capture the von Kármán spectra. The other methodologies (including the XCDF by Daniels *et al.* (2013)) do not have this drawback, and agree well with the validation data. The discrepancies between Daniels *et al.* (2013); Dagnew and Bitsuamlak (2014) can therefore be attributed to the local grid resolution, of which the grid by Daniels *et al.* (2013) is considerably finer. Unfortunately Dagnew and Bitsuamlak (2014) did not report the fluctuating pressure statistics for discussion.

Fig.12 shows the pressure statistics for the other inflow scenario. The wind tunnel measurements by Huang *et al.* (2005) are plotted alongside the numerical results of Yan and Li (2015); Daniels (2016) with various inflow generation methods. Again, the RFG inflow results show the largest discrepancy with the validation data. Better agreement can be seen with the Recycling and DSRFG methodologies, with an under-prediction of mean pressure for the lateral and leeward faces. Again, this can be attributed to the decay in energy for the higher frequencies in Fig.6. The Vortex and XCDF synthetic inflow methodologies show the better overall agreement with the target data, and resolve the von Kármán spectrum model over a wider range of frequencies. This is also seen for the fluctuating pressure statistics where these methods show more encouraging results. However, by their inconsistent distributions, it seems that the results for the other methodologies by Yan and Li (2015) are not fully converged.

Huang *et al.* (2007) investigated with CFD simulations the impact of velocity magnitude and turbulence intensities on the pressure statistics. They concluded that the mean pressure coefficients on the windward wall are very sensitive to the velocity profile but are not noticeably affected by the turbulence intensity. The mean pressure coefficients at the lateral and leeward walls are conversely more difficult to estimate, observing a noticeable disparity between the experimental and numerical results. Here, they state that the mean pressure coefficients on the lateral and leeward walls are sensitive to both the velocity magnitude and turbulence intensity, where the velocity profile is the dominating factor. These observations are consistent with those by Daniels *et al.* (2013) who also noted the statistics are largely insensitive to turbulent length scales, and increase proportionally with turbulence intensity.

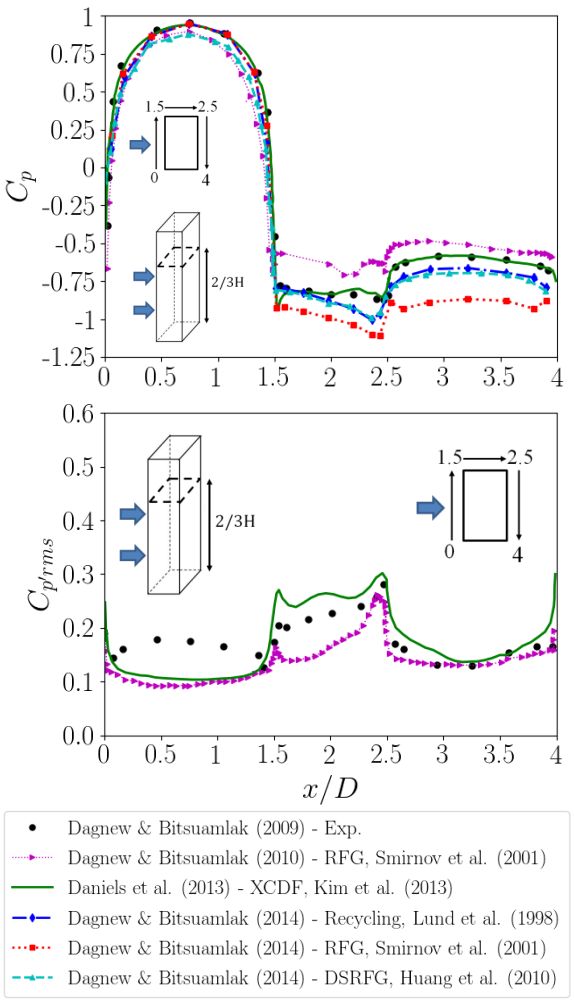

Figure 11. Comparison of inflow generation techniques for surface pressure statistics over the sides of the tall building model. Target inflow characteristics after the wind tunnel experiment of Dagnew and Bitsuamlak (2009).

Despite the extensive literature on the subject of wind loading on tall buildings, the authors' have noticed that an aspect that has not been considered in enough detail are the effects of the inflow conditions on the pressure distribution over the lateral faces. Figs.13-14 show the mean pressure contours over the lateral (left) side of the model for two mean velocity profiles. Regardless of the inflow condition, it can be seen for the mean pressure contours, there are two polarising regions at the top-left and bottom-right corners of the face. Another consistent characteristic of the mean pressure is the peak suction at the windward corner (left-side of the face), indicating a roll-up of the shear layer from the leading edge. For the smooth flow case, Fig.14, the mean suction pressure

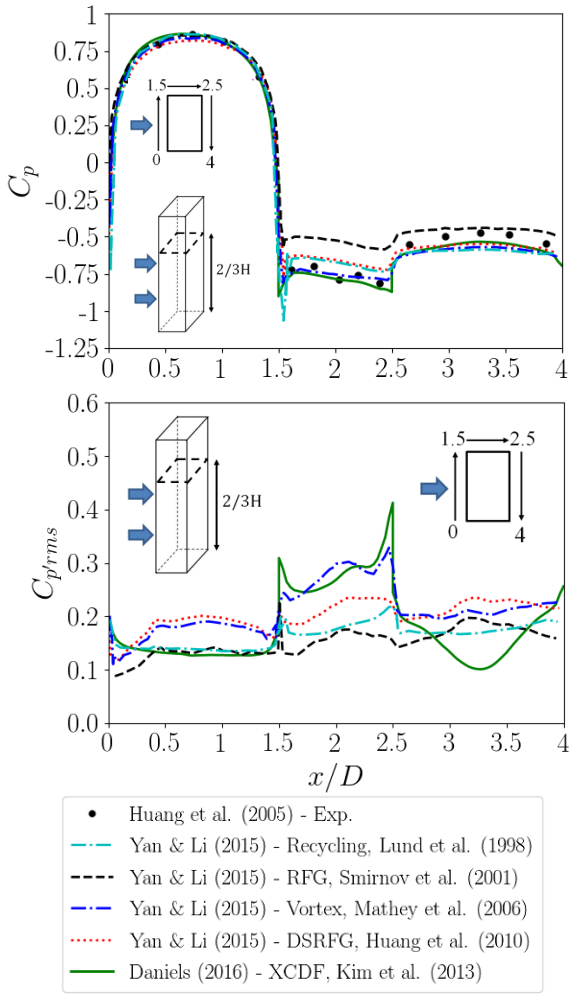

Figure 12. Comparison of inflow generation techniques for surface pressure statistics over the sides of the tall building model. Target inflow characteristics after the wind tunnel experiment of Huang *et al.* (2005).

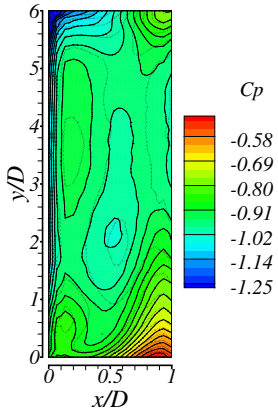

(a) C_p distribution for LES with $\alpha = 0.3$, base I_u and L_u (Daniels *et al.* (2013)).

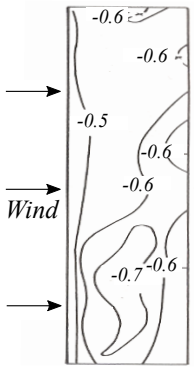

(b) C_p distribution over a tall model building for a 'boundary-layer' inflow velocity from a wind tunnel experiment. Redrawn from Baines (1963), (also Simiu and Scanlan (1978).

Figure 13. Mean pressure distributions over the lateral sides of a tall model building.

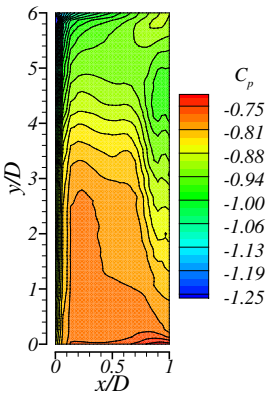

(a) C_p distribution for LES with $\alpha = 0.12$, smooth flow (Daniels *et al.* (2013)).

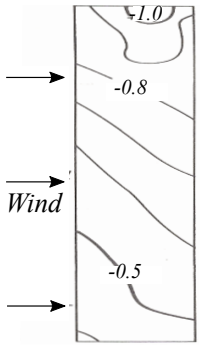

(b) C_p distribution over a tall model building for a'uniform' inflow velocity from a wind tunnel experiment. Redrawn from Baines (1963), (also Simiu and Scanlan (1978)).

Figure 14. Mean pressure distributions over the lateral sides of a tall model building.

can be seen to gradually increase towards the top of the model. For comparison to the LES results, Fig.13(b), and 14(b) shows one of the few experimental attempts in the literature plotting the mean pressure contour over the side face of a tall building model. In these figures, despite the tall building having a different aspect ratio to the CAARC tall building model, and having a slightly different inflow turbulence, some characteristic regions over the face are consistent with the LES results. Firstly, in Fig. 14, it can be seen that the *constant (uniform) velocity* profile has a similar 'layered' distribution of pressure to that of the LES data in smooth flow with the exponent $\alpha = 0.12$. The values of mean pressure monotonously increase towards the top of the model. This characteristic is unsurprising, considering that the LES results uses an exponent of $\alpha = 0.12$, corresponds to a steep profile at low altitude, would be expected to have a similar effect on the tall building to that of a 'uniform' flow. Secondly, in Fig.13, when the power law exponent is modified to $\alpha = 0.3$, introducing a more gentle velocity gradient at low altitude, the characteristic shapes show a similar profile to the *boundary-layer inflow* contour in Baines (1963).

Finally, effects of the inflow characteristics on the peak pressures on the lateral sides is of great interest. It has previously been demonstrated in Saathoff and Melbourne (1997); Daniels *et al.* (2013); Daniels (2016) that the effects of turbulence length scale and intensity on the magnitude of the surface pressure fluctuations becomes greater as the turbulence components increase. The peak recorded pressure, $C^*_{p'}$, is also expected to increase accordingly, defined as

$$C^*_{p'} = \frac{(p'^* - \langle p \rangle)}{0.5\rho U^2}, \quad (15)$$

where p'^* is the peak pressure extracted from a certain duration average. The experimental investigations of Saathoff and Melbourne (1997) and Li and Melbourne (1999) have already demonstrated this aspect for the surface pressures along a flat plate, particularly near the leading edge. From these observations, Saathoff and Melbourne (1997) proposed that $C^*_{p'}$ correlates well with the function

$$\eta^* = I_u \left(\frac{L_u}{B}\right)^{0.15}, \quad (16)$$

where B is the thickness (flow-normal projection) of the plate. Due to limitations of the experimental set-up, only a small range of $0.08 \leq \eta^* \leq 0.21$ was investigated in their work with suitable agreement. Thus applying this function to the results of Daniels *et al.* (2013), extending this range towards $\eta^* = 0.39$, would be beneficial in demonstrating the consistency of this function. Furthermore, while this function was originally suggested for the peak pressure towards the leading edge, the present work would apply this function to the probe data at the leading edge of the model building. The obtained peak pressure from the time series data, $C^*_{p'}$, was normalised by the freestream velocity at the corresponding height of the probe.

Fig.15 shows peak pressure data from Saathoff and Melbourne (1997) and the CAARC building data to the function η^*. The probe data at the leading edge of the model was sampled along the height of the model. From the numerical data in various inflow conditions, the figure shows that despite the interference of 'end-effects' and a slight scatter of results for some cases, a linear progression can be identified with a consistent trend to the data of Li and Melbourne (1995). The smooth flow data by Daniels *et al.* (2013) indicate an interception of this trend with the y-axis at approximately $C^*_{p'} \sim 0.6$, showing that even in the case of the smooth flow, a peak suction pressure can be attained at the leading corner. Furthermore, for the case of doubling the turbulence intensity, the LES results show that the function proposed by Saathoff and Melbourne (1997) is still consistent for cases of large-scale turbulence.

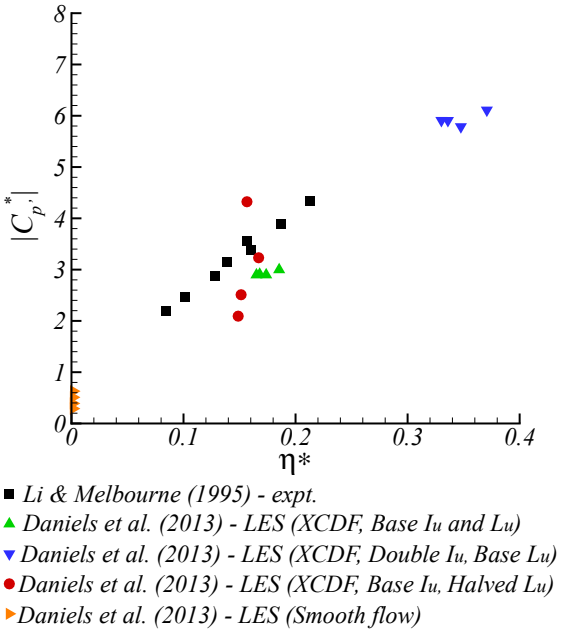

Figure 15. Maximum recorded value of the peak pressure coefficient at the leading edge as a function of the turbulence parameter, η^*. Diagram source: Daniels (2016).

6. Vortex-Induced Vibrations of bridge sections

The fluctuating pressures around a structure, generated by the periodic vortex shedding in the wake, result in a cross-wind force characterised by a dominant frequency described by the Strouhal number $Str = f_s D/U$, where f_s is the dominate frequency component of the vortex-induced force; D is the flow-normal projection thickness of the structure; U is the oncoming flow velocity. As the frequency of vortex-induced forces approaches the modal frequency of the bluff body, a resonant response, denoted *'Vortex-Induced Vibration (VIV)'*, *'lock-in'*, or *'synchronisation'* is observed. At the occurrence of VIV, the amplitude of oscillation increases, and the structure's motion dominates the surrounding fluid motion. This particular aeroelastic phenomenon leads to the violation of Strouhal's law; specifically, the frequency of the structure dictates the formation of vortices in the wake. A significant change in surface pressures (and peak loading) are observed over the structure during this phenomenon (Daniels (2016); Nguyen *et al.* (2018)). Although the VIV response does not always result in catastrophic failures, it can seriously impact the fatigue life and a loss of desired functionality of the structure. To eliminate a VIV response, devices such as fairings, or flaps are implemented to distort the periodic vortex shedding around the structure, thus mitigating the effects of VIV. These design alterations are typically developed through wind tunnel experiments.

6.1. Wind tunnel analysis

For wind tunnel tests, rather than examine the complete structure, the aerodynamics of the bridge can be studied by constructing a model that represents the short, mid-span, cross-section of the deck.

This approach has shown to be just as effective in the aeroelastic analysis of bridges to that of the full-span model (Wardlaw (1980)). The sectional model is simple in structure, hence it can reduce the wind tunnel test cost accordingly, compared to the full-span equivalent. An example of both setups is shown in Fig.16.

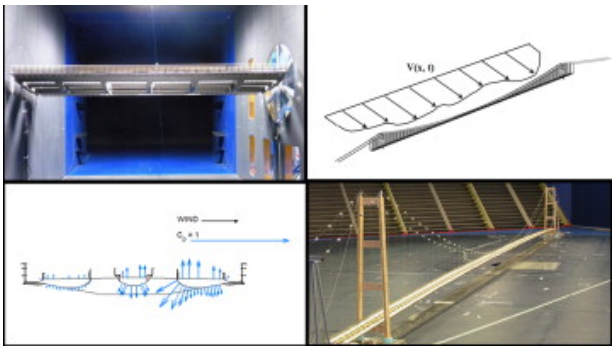

Figure 16. Experimental setups for the full-span and sectional model testing of a bridge. Diagram source: Diana *et al.* (2013).

It is typical in the literature to examine VIV aerodynamics through a bridge deck with a rectangular cross-section, as this represents a common geometry for a structural member. The elastically-supported rectangular cylinder is prone to VIV due to the impinging Motion-Induced Vortex (MIV) shed from the leading edge or the von Kármán vortex street from the trailing edge (Mills *et al.* (2002); Matsumoto *et al.* (2008)) as indicated in Fig.17. For a range of depth-to-width ratio (B/D) from 2.6 to 8, these mechanisms are indistinguishable. In addition, different harmonics of the VIV can be observed, which are associated with different numbers of vortices present along the surface of the body due to the long after-body length. This characteristic also makes this geometry susceptible for the resonance response to interact with other aeroelastic phenomena (see Mannini *et al.* (2014)).

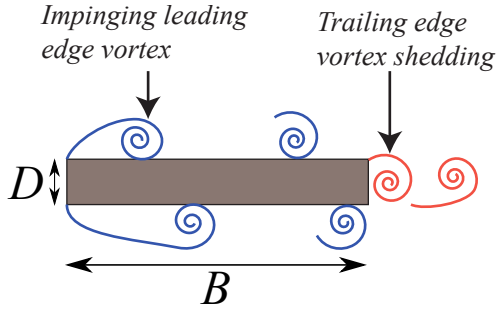

Figure 17. A sketch of the vortex formation around a rectangular cylinder with $B/D \geq 4$.

Nakamura and Mizota (1975) conducted a series of wind tunnel experiments on spring-mounted rectangular cylinders of different aspect ratios. Under a prescribed (forced) motion, the base pressures and lift-force data suggested an enhancement in vortex-induced effects with decreasing aspect ratio of chord-length (B) to width (D). A VIV response was observed regardless of the aspect ratio, with a prominent 'lock-in' region for each case. In addition, Nakamura and Mizota (1975) speculated on the physical mechanisms of 'lock-in' phenomenon. The abrupt phase change of the unsteady lift force, which closely correlated with the phase change of the near-wake velocity field, resulted in negative aerodynamic damping near the 'lock-in' range, which lead to large response amplitudes. Similar observations have been reported for circular cylinders (Bearman (1984)).

Komatsu and Kobayashi (1980) carried out a series of experiments on elastically-mounted cylinders with various cross-sections, such as the L-shaped, T-shaped, H-shaped, and rectangular with different aspect ratios. Both free and forced (sinusoidal) heaving oscillations were used together with the smoke-wire flow visualisation technique. It was observed that the von Kármán vortex street (generated from the trailing edge) and MIVs (from the leading edge) were the two main sources of VIV. They also suggested an empirical formula for the critical wind velocity corresponding to the maximum VIV response – a linear function to the aspect ratio of bluff cylinders.

Shiraishi and Matsumoto (1983) conducted a similar study on cross-sections such as rectangular, H-shaped, trapezoidal and hexagonal in both heaving and torsional Degrees-Of-Freedom (DOF). Three generation mechanisms of VIV were identified: separated vortices from leading edge due to structural motion, secondary vortices at trailing edge also due to structural motion, and separated vortices from trailing edge due to von Kármán vortex street. Various aspect ratios were investigated in this study. The results indicate that bridge decks with long after-body are more effective in mitigating the effects of VIV.

The studies above outline the early attempts to understand the aerodynamics of a structure undergoing a VIV response. However, the inability to measure the surface pressure (loading) on a structure undergoing VIV is a fundamental drawback for the wind tunnel, which conducts the aeroelastic analysis using one of two methodologies: The *forced vibration method* measures and compares pressures over the model which is subjected to prescribed (sinusoidal) motion (e.g. Ricciardelli (2010)); alternatively, the *free vibration method* interpolates the aerodynamic forces indirectly by measuring the motion of the model supported elastically and driven by the fluid-structure interaction (e.g. Marra *et al.* (2015)). Very few contributions to literature compare the characteristics between the two approaches. It can be deduced that the forced vibration test clearly omits the memory effects of the fluid from the previous oscillatory cycle. It is therefore intuitive that there may be some differences between the methods for the aerodynamic forces. In cases where this is compared, it is generally agreed that there are

considerable discrepancies in the phase angle between the response of the structure and the aerodynamic forces (Jamal and Dalton (2005); Placzek *et al.* (2008); Marzouk (2011)). Moreover, wind tunnel experiments from the literature are somewhat limited on visualising the flowfield over the lock-in regime. This technique has become more popular in the last decade with the advancement of modern techniques to record the deflection over time (e.g. Marra *et al.* (2011); Andrianne (2012)). However, obtaining accurate data for the simultaneous measurement of deflection and aerodynamic forces has shown to be troublesome, leading to substantially large calibration errors (e.g. Ricciardelli *et al.* (2002); Vandiver *et al.* (2009)). It is therefore likely that a confident assessment for the aerodynamic forces over a freely vibrating body is not in the scope of the wind tunnel for the immediate future. Consequently, the aeroelastic test has been applied in the context of numerical methods, namely CFD with the attempt of reproducing the wind tunnel experiment.

6.2. CFD analysis

Like the wind tunnel, the interest in simulating flows over rectangular cylinders has grown rapidly over the past few decades. This is largely due in part to the introduction of benchmark studies (e.g. BARC, Bruno. *et al.* (2014); Mannini *et al.* (2019)) which aim to examine the aerodynamics around elongated bluff geometries. Concurrently, a number of attempts have been made to examine the aerodynamics of an elastically-mounted rectangular cylinder. The Fluid-Structure Interaction (FSI) between the cylinder and the surrounding fluid is typically achieved through an explicit conventional staggered algorithm (see Jaiman *et al.* (2011); Daniels and Xie (2015)). As the experimental setup consists of a discrete mass-spring-damper system, the structural response is thus modelled through an Ordinary Differential Equation using an external force determined from integrating the surface pressure over the geometry. Examples of this setup using LES to model the fluid turbulence include Sarwar *et al.* (2008); Sun *et al.* (2008, 2009); Sarwar and Ishihara (2010); Bai *et al.* (2013); Zhu and Chen (2013); Daniels *et al.* (2016); Nguyen *et al.* (2018); Álvarez *et al.* (2019); Chen *et al.* (2019). These articles highlight the suitability of LES to capture the inherent unsteadiness in FSI problems and to maintain the flow structure in the wake region in contrast to the over-dissipative nature of URANS modelling (e.g. Shimada and Ishihara (2002, 2012)). Fig.18 shows the equivalent CFD and wind tunnel setup of the aerelastic analysis of a rectangular bridge section.

7. Numerical studies on the mechanisms of VIV for rectangular cylinders

In many cases of VIV analysis, CFD data has been complementary to the equivalent wind tunnel study. More recently, this aspect has been reciprocated. Marra *et al.* (2011, 2015) carried out a series of wind tunnel measurements for the VIV response amplitude of an elastically-mounted rectangular cylinder, varying the structural damping of the system for each case. The response of the structure undergoing a resonant response is inversely proportional to the square-root of the effective damping ratio (structural plus aerodynamic). An important number to characterise the response amplitude of a fluid-induced oscillating body is the Scruton number Sc (see Hansen (2013)). This number is proportional to the structural damping and to the ratio between the mass of the vibrating structure and the mass of the fluid displaced by the structure. Higher values of Scruton numbers indicate a lower response amplitude of oscillation. For the heaving DOF, this number, based on the logarithmic decrement δ or structural damping ζ, is defined:

$$Sc = \frac{2m\delta}{\rho BD} = \frac{4\pi m\zeta}{\rho BD}, \tag{17}$$

where m is the mass per-unit-length of the structure. The work by Marra *et al.* (2011, 2015) therefore provides benchmark data for validating CFD techniques for modelling VIV, as well as providing a basis for new analytical models relating the response amplitude of a body with the Scruton number. The wind tunnel data by Marra *et al.* (2011) has already been employed for this purpose using LES (Daniels *et al.* (2016); Nguyen *et al.* (2018); Álvarez *et al.* (2019)).

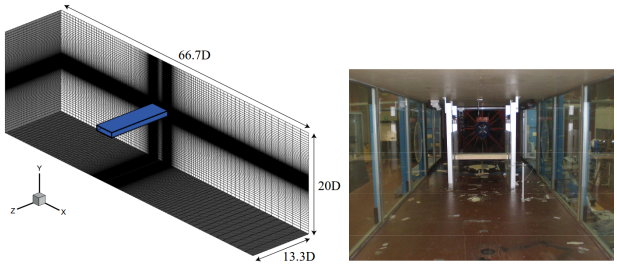

(a) CFD domain setup for LES in Daniels *et al.* (2016).

(b) Aeroelastic Wind-Tunnel configuration. Photo source: Marra (2011).

Figure 18. Equivalent CFD and aeroelastic wind tunnel setups for the analysis of VIV of a spring-mounted rectangular cylinder.

Response amplitudes for a rectangular cylinder with aspect ratio $B/D = 4$, and $Sc = 6$ from the literature are plotted in Fig.19. These include the wind tunnel data by Marra (2011), and the equivalent LES results by Daniels *et al.* (2016); Álvarez *et al.* (2019). Marra *et al.* (2011) repeated their experiment twice with small differences of amplitude for $U/f_nD > 8.5$. The first test data (labelled 'Series 1' in their paper) is plotted here. For simulated flows around rectangular cylinders, the most influential parameters for the surface pressure is the grid resolution along the span (Δz). As determined from several authors on a fixed cylinder, this resolution should be within the range $\Delta z/D \leq 0.1$ in order to obtain a suitable prediction of the spanwise correlation of pressure (e.g. Tamura *et al.* (2008); Bruno *et al.* (2010, 2012)), as well as suitable pressure statistics (Nguyen *et al.* (2018)). For an elastically-mounted cylinder, the repercussions of a poor spanwise resolution can be seen in Fig.19. Álvarez *et al.* (2019) also

increased the resolution in the surrounding grid (such as the wake region - *'finer grid'*) resulted in a closer agreement to the target experimental data. The LES results from Daniels *et al.* (2016), using a finer spanwise grid resolution, resulted a closer agreement with the target wind tunnel data.

It can also be seen in Fig.19 that the on-set reduced velocity of the lock-in region is largely insensitive to the grid resolution, with all LES results showing a later onset of lock-in with respect to the experimental data; this can be attributed to the subtle differences in the predicted value of the Strouhal number between the experimental setup and the simulations. While overall this validation seems promising, it should be noted that in order to achieve the necessary grid resolution, a supercomputer is required to carry out the computation - rendering this infeasible for industry. Alternatively, the span could be reduced to a length $\sim B$, and periodic or symmetric boundary conditions could be employed (Nguyen *et al.* (2018)).

As previously mentioned in this article, an appealing feature of CFD (compared to the wind tunnel) is the flowfield data can be easily extracted from the domain. As such, the aerodynamic loading, wake velocities can be measured during oscillation and provide a deeper insight in the aerodynamics of the cylinder.

The dominant frequencies of the aerodynamic lift, wake velocity, and response amplitude over the lock-in region are plotted in Fig.20. Between the reduced velocities $7.5 \leq U_r = U/f_n D \leq 8.5$ (lock-in), the frequencies of the structural response and aerodynamics is locked into the natural frequency of the structure (f_n). After this region $U_r \geq 8.5$, the response amplitude remains equal to the natural frequency of the system, while the aerodynamic lift force frequency follows the vortex shedding frequency (f_s) defined by the Strouhal's law ($Str = f_s D/U$). The termination of the lock-in region coincides with the instance when the lift force and vertical displacement phase-lag angle is approximately 180° (Nguyen *et al.* (2018)). It can be seen that the for reduced velocities lower than the lock-in region ($U_r \leq 7.5$), the amplitude response, and aerodynamic lift is dominated by the vortex-shedding frequency (Strouhal's law). The same trends were observed by Álvarez *et al.* (2019) (Fig.21), who also stated that the effects of the spanwise grid resolution significantly affects the aerodynamic lift prediction, and the resulting lock-in region. Special care is therefore needed when constructing the grid so as to accurately capture the pressure statistics. This could be achieved through initial tests on the equivalent fixed cylinder (Daniels (2016); Nguyen *et al.* (2018)).

Fig.22 shows the time series for the aerodynamic lift and response amplitude at various reduced velocities around lock-in. In agreement with Figs.20 and 21, it can be seen in this figure that the phase difference between the response displacement and lift changes depending on the flow regime around lock-in. For the reduced velocities below the onset of lock-in, $7.5 \leq U_r$ (Fig.22(a)),

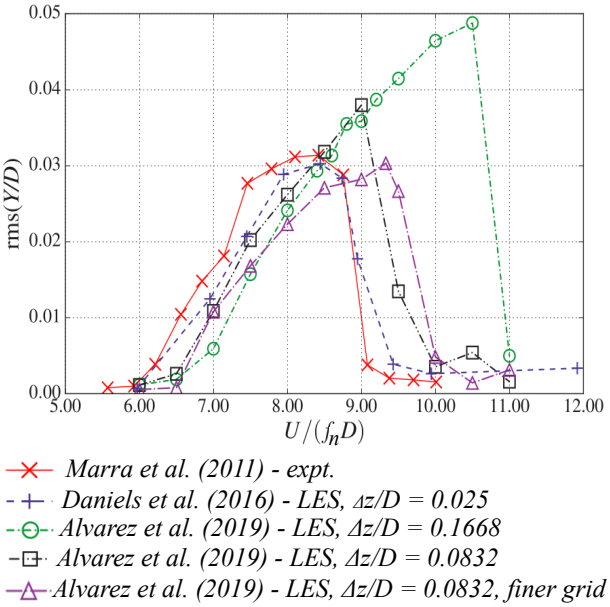

Figure 19. Comparison of experimental and LES results from the literature for the non-dimensional deflection versus reduced velocity of a rectangular cylinder in smooth flow (f_n =vertical natural frequency, Δz the grid size along the span). Diagram source: Álvarez *et al.* (2019).

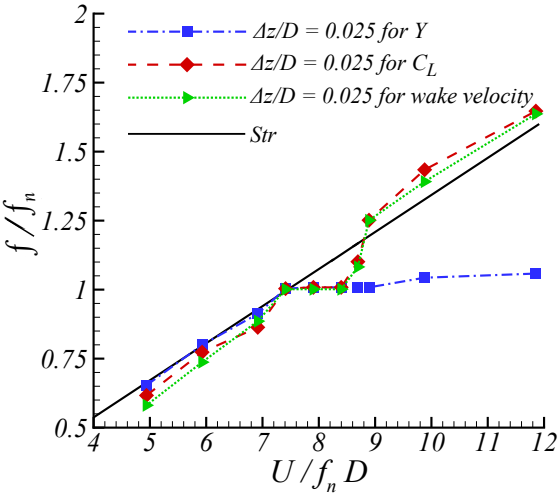

Figure 20. Dominant frequency for the response amplitude, lift coefficient (C_L), and wake velocity for an elastically-mounted rectangular cylinder undergoing heaving oscillations over the lock-in region ($7.5 \leq U/f_n D \leq 8.5$). Strouhal's law is defined, $U = f_s D/Str$. Diagram source: Daniels (2016).

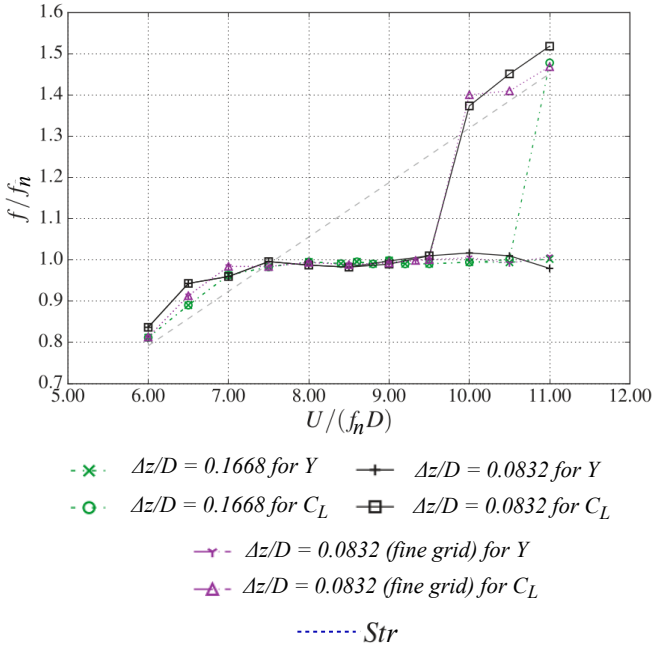

Figure 21. Dominant frequency for the response amplitude, and lift coefficient (C_L) for an elastically-mounted rectangular cylinder undergoing heaving oscillations over the lock-in region ($7.5 \leq U/f_nD \leq 8.5$). Diagram source: Álvarez *et al.* (2019).

the response displacement and lift force can generally be seen to fluctuate at the same frequency (also indicated in Fig.20), resulting in a phase difference of approximately 0° (with some intermittent deviations). It can be deduced from this that the response of the structure is dominated by the lift force in this flow regime – following Strouhal's law. At lock-in (Fig.22(b)), the dominant frequency of the lift force is synchronised with the resonant frequency of the structure. It can also be seen that the lift force is enhanced in this region, with the statistic for fluctuation $C_{L,r.m.s} = 0.42$. For reduced velocities larger than lock-in region, $8.5 \leq U_r$, Figs.22(c)-22(d), the aerodynamic lift begins to deviate from the motion of the structure. For Fig.22(c), the lift force intermittently fluctuates between in-phase and out-of-phase with the structure's motion. As the reduced velocity increases the statistics for the lift force is as for the equivalent static case ($C_{L,r.m.s} = 0.2$,Guissart *et al.* (2019)), the frequency of the lift force also increases - following Strouhal's law again. It can be deduced from this that at post lock-in, the aerodynamic lift force and the response act independently from each other. This increase in aerodynamic lift agrees with the observations by Ricciardelli (2010) through wind tunnel experiments using forced oscillations for the cylinder.

Wind tunnel visualisation of the flowfield while the cylinder is undergoing VIV has been attempted by a few researchers (e.g. Naudascher and Wang (1993), Andrianne (2012)). In their

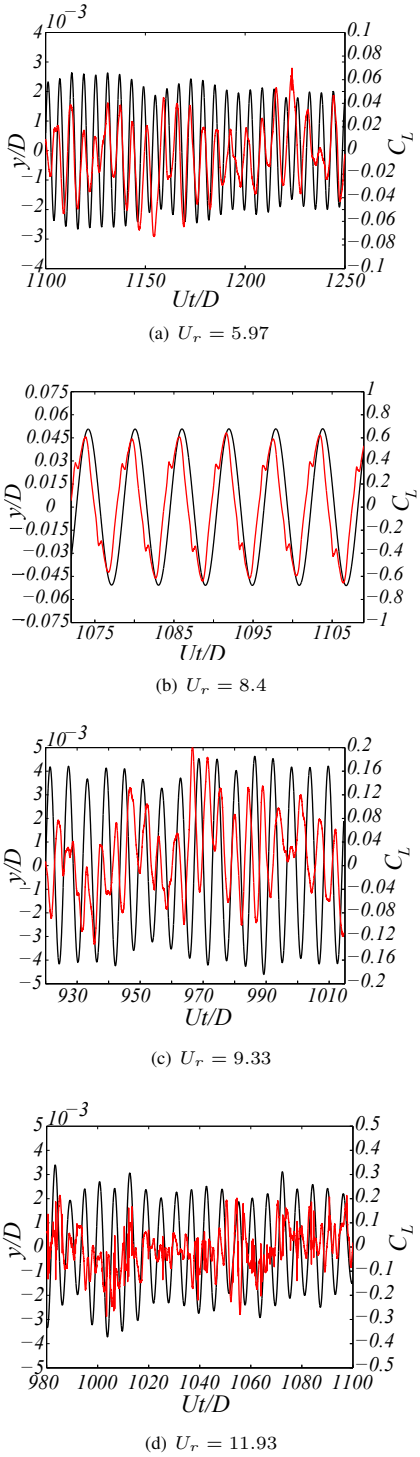

(a) $U_r = 5.97$

(b) $U_r = 8.4$

(c) $U_r = 9.33$

(d) $U_r = 11.93$

Figure 22. Time series of the lift and heaving response displacement for various reduced velocities ($U_r = U/f_nD$). The lift coefficient is defined: $C_L = L/0.5\rho U^2 B$, where L is the lift force. Diagram source: Daniels (2016).

pioneering work, Komatsu and Kobayashi (1980) identified the formation of the leading edge (motion-induced) vortex during each cycle. An appealing aspect of their work is the simultaneous measurements of pressure and the visualisation of the vortex formation (via a smoke-wire method). However, it would be challenging to measure the surface pressure when the leading edge vortex is very strong during the up/downstroke in experiments. LES, in contrast, does not suffer from such a technical limit. Thus, a comparison of the predicted flowfield and surface pressure distributions between Komatsu and Kobayashi (1980) and the LES results of Daniels *et al.* (2016) would provide a deeper insight into the consistency of the two methods in the study of such aeroelastic phenomena. The top of Figs.23(a)(i) and 23(b)(i) show the predicted vortex formation by Komatsu and Kobayashi (1980) for the cylinder at a peak upward deflection (Fig.23(a)), and neutral position (Fig.23(b)) during the down-stroke motion. The LES results are shown underneath each diagram with the identified vortices highlighted in blue. In their work, Komatsu and Kobayashi (1980) note:

1. The formation of the vortex from the leading edge, 'A' synchronises with each cycle of the cylinder's motion.
2. Vortex 'A' keeps growing during each cycle (vortex 'B') and subsequently convects to the trailing edge (vortex 'E') into the wake.
3. Vortex D' produces a downward lift force greater than the upper surface.

Similar conclusions have been made for the LES results, hence, the simulated sequence presented here is consistent with the explanation of the vortex formation over the cylinder described by Komatsu and Kobayashi (1980). Their forced oscillation tests were carried out with a maximum displacement (y/D) set to 0.066, which was smaller than that of the LES for $Sc = 3$; this could account for the formation of a secondary vortex in the LES flowfield, which is not observed in theirs. Nevertheless, the combined pattern of the primary and secondary vortices is in a reasonable agreement with the predicted pattern by Komatsu and Kobayashi (1980). Despite this agreement, the pressure distributions between these two works show considerable disparity. While their observations indicate that the phase between the response displacement and aerodynamic lift is $90°$, a major difference to the LES prediction is the source of excitation. Komatsu and Kobayashi (1980) suggest that the MIVs convecting along the upper and lower surfaces produces the greatest contribution to the aerodynamic lift force (in a similar way to the flow over a static body in smooth flow, see Daniels (2016)), rather than its formation at the leading edge. The LES results disagree with this. In the same publication, the surface pressure statistics in Komatsu and Kobayashi (1980) indicate a contradiction, showing a peak suction pressure towards the leading edge of the cylinder, which is similar with the characteristics of the surface pressure discussed in Daniels *et al.* (2016) and Daniels (2016).

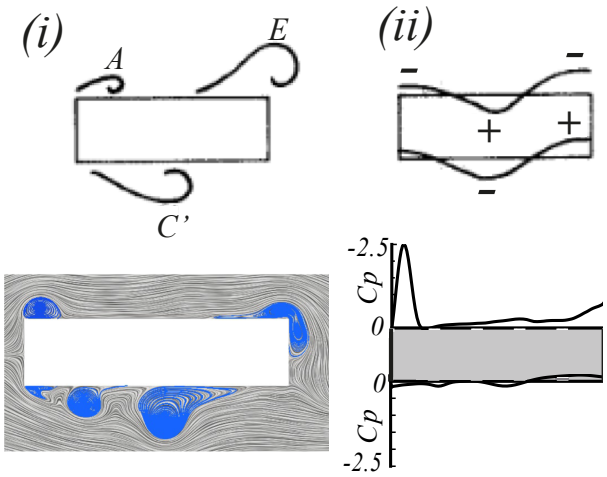

(a) Peak amplitude on the upward deflection.

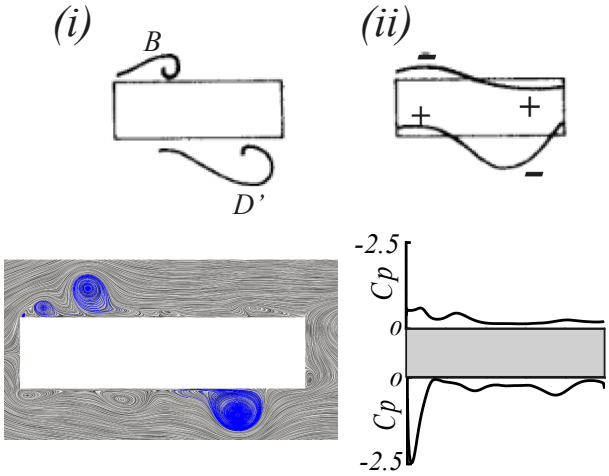

(b) Neutral position during the down-stroke motion.

Figure 23. (top of each figure) Komatsu and Kobayashi (1980)'s description of the (i) vortex pattern and (ii) pressure distribution for a freely vibrating rectangular cylinder at $U_r = U/f_n D$ slight greater than $1/Str$. (bottom of each figure) the equivalent LES results from Daniels (2016) for $U_r = 8.4$ with $Sc = 3$. Diagram source (top of each figure): Komatsu and Kobayashi (1980).

Despite potentially incurring larger amplitudes, wind tunnel results for the torsional DOF are not as common as those observed for heaving. The Scruton number for the torsional motion is defined:

$$Sc = \frac{2I\delta}{\rho D^4} = \frac{4\pi I\zeta_t}{\rho D^4}, \tag{18}$$

where I is the mass moment of inertia per-unit-length of the structure. Like the wind tunnel, numerical modelling of the torsional responses of a bridge section are also extremely scarce. A notable contribution to the understanding of torsional flutter is

provided by the works of Matsumoto (e.g. Matsumoto (2009)). Matsumoto has clarified the effects of von Kármán vortices on torsional flutter, such as torsional mitigation (Matsumoto *et al.* (2003)). However, it must be noted that a large portion of this topic is still not yet understood, such as the characteristics of the aerodynamic forces at this occurrence, let alone the mechanism of von Kármán vortices on the flutter stability. With the features associated with CFD and its fast development, detailed analysis of this motion becomes feasible, and will be very useful for the further understanding of this topic.

The pitching response (with $Sc = 7.862$) determined through LES by Daniels *et al.* (2016) is shown in Fig.24. The numerical results show a close agreement with the equivalent wind tunnel data of Matsumoto *et al.* (2008) for VIV response, located at reduced velocity $U_r = U/f_t D = 5.1$. The location of this peak response is in agreement with the guidelines by Shiraishi and Matsumoto (1983), who suggested the locations of a VIV response to be approximately two-thirds of the inverse Strouhal number ($Str = 0.136$). However, there is some discrepancy for the onset of the lock-in region, which may be attributed to the differences in the prediction of Strouhal number, as described for the heaving case.

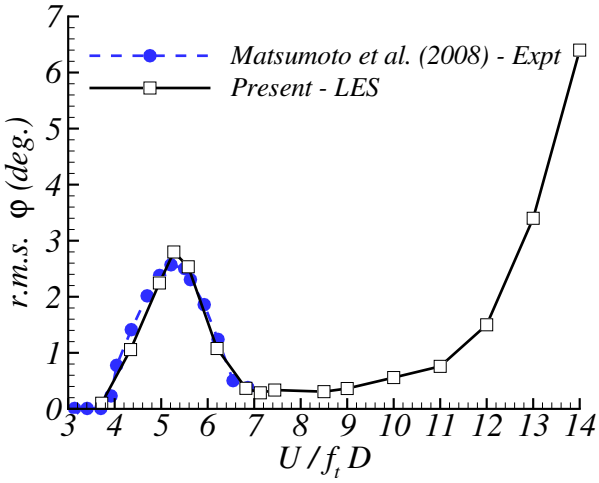

Figure 24. Root-mean-squared values of the r.m.s. pitching angle versus reduced velocity (f_t = torsional natural frequency), with the rotational axis around mid-chord. Diagram source: Daniels *et al.* (2016).

Fig.25 shows the streamlines around the cylinder, and the resulting pressure distribution over the lateral faces during one period of oscillation at reduced velocity $U_r = 13$ - corresponding to the incipient torsional flutter. It can be seen that the phase difference between pitching moment coefficient and the motion of the cylinder is approximately 0^0 (in-phase) when approaching torsional flutter. Consequently, the MIV is now formed when the cylinder is at its neutral position as opposed to its peak amplitude. The mean convection velocity of the MIVs, U_c, were calculated by the phase changes of pressure along the cylinder's chord (see Daniels (2016); Nguyen *et al.* (2018)). This convection velocity in the lock-in regime for the torsional motion was deduced to be approximately 60% of the freestream velocity, which is in agreement with the estimate by the equivalent wind tunnel experiment of Matsumoto *et al.* (2008).

In Fig.24, it can be seen that the $r.m.s.$ pitching angle begins to diverge beyond reduced velocity $U_r = 10$. Thus, for this case, the reduced velocity for the onset of torsional flutter is approximately twice that of the reduced velocity for the lock-in region ($U_r = 5$). To the best of the authors' knowledge, validation data of the pitching angles beyond reduced velocity $U_r = 10$ is not reported in the literature. In such cases many researchers rely on simplified models to predict the critical freestream velocities in which the body will undergo torsional flutter.

Analytical predictions for the onset of torsional flutter has been in continual development over the last few decades. To recall the expression for the onset of torsional flutter in Eurocode (2005),

$$U_{div} = \sqrt{\frac{2k_\alpha}{\rho B^2 \frac{\partial C_M}{\partial \alpha}}}\ , \tag{19}$$

where k_α is the torsional stiffness, and $\partial C_M/\partial\alpha$ is the gradient of the pitching moment with respect to the angle of attack. Applying this expression to the present case, the value of reduced velocity for the onset of torsional flutter is $U_r = 14.3$. This is arguably in agreement with the available LES results. Several researchers have attempted to develop simplified stability criteria for the onset of torsional flutter based on phenomenological observations (e.g. Shiraishi and Matsumoto (1983), Larson and Larose (2015)). Shiraishi and Matsumoto (1983) suggests that the onset of torsional flutter is $U_r = 2/Str$, based wind tunnel measurements, which when applied is calculated as $U_r = 13.98$. In a later publication, Matsumoto *et al.* (2008) carried out the same assessment, resulting in the following expression:

$$U_r = \frac{U_C}{f_t D} = \frac{2}{2N-1} 1.67 \frac{B}{D}, \tag{20}$$

where $N = 1, 2; ....$ Substituting $N = 1$ into Eq.20 one finds the critical reduced velocity to be $U_r = 13.36$. Despite the continuing development of these simplified models, what seems to be lacking in the literature is a consistent definition for the '*onset*' of torsional flutter, and is thus left open to interpretation. A discussion of this aspect, presented by Larson and Larose (2015), is based on the convection velocities of the MIVs of the upper and lower surfaces of the cylinder, when undergoing forced pitching oscillations; in their work, it is stated that no torsional flutter instability occurs when the distance of the MIV along the chord between the upper surface and the lower surface is higher than the half width of the cylinder ($B/2$). To verify this, the authors propose to apply this simplified model to LES results from the literature. As indicated in Daniels

et al. (2016); Nguyen *et al.* (2018), the MIV is generated on the upper surface, at the beginning of each oscillatory period (neutral position), hence the aforementioned condition is equivalent to

$$T_C > T_t/2, \tag{21}$$

where T_t $(= 1/f_t)$ is the period for one cycle of the structure's oscillation, and T_C is the time for the MIV to convect along the chord. Using the non-dimensional reduced velocity based on the chord $U_{red,B} = U/f_tB$, the condition above yields,

$$T_C > \frac{BU_{red,B}}{2U}. \tag{22}$$

By analysing the phase changes in pressure over the cylinder during each cycle (see Daniels (2016)), the convection velocity, U_C, of the MIV for the incipient torsional flutter ($U_r = 10$) was deduced to be approximately 28% of the freestream velocity. Furthermore, for reduced velocity $U_r = 14$, the convection velocity was found to be 25%, i.e. $U_C = 0.25U$, hence

$$U_CT_C = \frac{B}{2} \rightarrow 0.25UT_C = \frac{B}{2} \rightarrow T_C = \frac{B}{0.5U}. \tag{23}$$

Combining Eq.22 with Eq.23 results in the expression,

$$\frac{B}{0.5U} > \frac{BU_{red,B}}{2U} \rightarrow U_{red,B} < 4. \tag{24}$$

The resulting critical freestream velocity corresponds to the equality

$$U_{red,B} = \frac{U_C}{f_tB} = 4 \text{ or } U_r = \frac{U_C}{f_tD} = 16. \tag{25}$$

In Larson and Larose (2015), dealing with the failure of the Tacoma Narrows bridge, the convection velocity of the MIVs was identified to be 25%- 27% of the oncoming freestream velocity. Hence the resulting minimum critical reduced velocity (Eq.25) is expressed,

$$U_{red,B} = \frac{U_C}{f_tB} = 3.7, \text{ or } U_r = \frac{U_C}{f_tD} = 14.8. \tag{26}$$

The model proposed by Larson and Larose (2015) requires the *a-priori* knowledge of the convection velocities of the MIV which may not be consistent for all cases, considering the sensitivity of the vortex formation to geometric details of the structure. Finally, in essence of the formula provided the Eurocodes, it has been suggested that the expression for torsional flutter should be a function of the structural properties (i.e. the Scruton number) (Andrianne (2012)), though (to the best of the authors' knowledge) this has not been investigated in the literature. Nevertheless, the LES results and discussion demonstrate the appealing aspects of LES in aiding for describing the physics of an inherently complex flow problem.

7.1. Freestream turbulence effects on the amplitude of VIV response

Further studies on the buffeting response of an elastically-mounted bluff body have shown a significant effect of the turbulence on the pressure distribution and aeroelastic behaviour. Matsumoto *et al.* (1993) reported the turbulence-induced stabilisation effect on the VIV of the rectangular cylinder, due to an increase in the vorticity diffusion and thus a decrease in the strength of vortices. However, Wu and Kareem (2012) and Kareem and Wu (2013) have recently discussed the deficiencies of the quantitative and qualitative understanding of the turbulence-induced effects of VIV on a generic (e.g. circular) and bridge-deck cross section, and the considerably less number of studies on the latter than those on the former. Cao *et al.* (2017) reviewed a number of cases for the circular cylinder. They suggested that turbulence has a very strong influence on the extension of the lock-in region, and in some cases, turbulence can completely suppress the structure's response. In opposition to this, the wind tunnel study by Goswami *et al.* (1993) suggested that the variation of the response amplitude of a freely-vibrating circular cylinder in turbulent flow was minimal, compared to that measured in smooth flow. As for bridge-deck cross sections, including the rectangular cylinder, Kobayashi *et al.* (1990, 1992a); Matsumoto *et al.* (1993); Kawatani *et al.* (1993, 1999); Haan (2000) conducted a series of wind tunnel tests investigating the response of rectangular and hexagonal cylinders of various aspect ratios in smooth and turbulent flows. The turbulence suppression effect was observed for the rectangular cross-sections, but not for the hexagonal ones. Wu and Kareem (2012) suggested that this was due to the difference in the mechanism of the VIV – whether the VIV was driven by the MIV or von Kármán vortex (see Fig.17). In a scenario that freestream turbulence does not affect the MIV, the response amplitude could be increased since the turbulence weakens the von Kármán vortex and its mitigation effects on the MIV (Matsumoto *et al.* (2008); Wu and Kareem (2012)). Nevertheless, more studies are required to clarify these inconsistencies and provide a more comprehensive explanation on the mechanism of turbulence-induced effects on the MIV and resulting VIV.

There are many cases where the VIV responses, estimated in wind tunnel tests, are not observed in full-scale bridges (Owen *et al.* (2013)). Many researchers suggest that these are owing to the difference of the turbulence in natural wind and in wind tunnel (e.g. Utsunomiya *et al.* (2001)). Typically, the turbulent scales observed in wind tunnel tests are usually too small to estimate its effect of a full scale bridge. The grid perturbation techniques employed in these works generate freestream turbulence with length scales being the dimensions of the structure. It can be seen that the actively controlled techniques increase the streamwise length scales to be close to the scales observed in atmospheric turbulence and specified by the Eurocodes (i.e. Eurocode (2011)). However, these are somewhat limited for the components in the vertical and spanwise directions. Generally, in all the listed papers, the focus of these

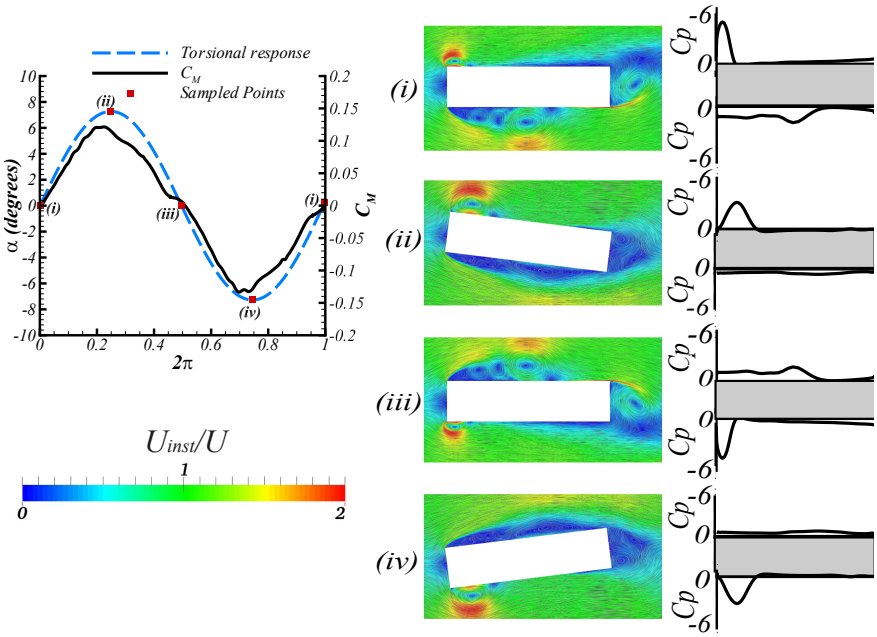

Figure 25. Streamlines and pressure distribution over the cylinder during one cycle at the incipient torsional flutter ($U_r = U/f_t D = 13$) for 1DOF pitching with rotation around the mid-chord. Left: pitching moment and angle phase-averaged time series over one cycle, with $C_M = M/0.5\rho U^2 B^2$. (i)-(iv) correspond to each quarter cycle. Diagram source: Daniels (2016).

works are on the response of the cylinders with varying parameters of the turbulent flow (e.g. intensity and integral length scales). It is generally agreed among these works that increasing the turbulence intensity reduces the structural response (thus agreeing with the speculation of Naudascher and Wang (1993)), while increasing the length scales of the flow has an enhancing effect. However, very little discussion is presented in these works on the mechanism for these responses. This is largely due to the limited ability to provide such insights.

Analysis into the effects of freestream turbulence on the response amplitudes and flowfield for the heaving motion were performed by Daniels *et al.* (2016) using LES, utilising the aforementioned XCDF inflow condition by Kim *et al.* (2013). Fig.26 shows the ratio of the peak response between the turbulent and smooth flows ($(R_y = y_{turb.}/y_{smooth})$) with varying the streamwise intensity component I_u (a), and the integral length scale L_u (b) for the heaving motion at reduced velocity $U/f_n D = 8.4$. The wind tunnel results of Kobayashi *et al.* (1992b) with aspect ratio $B/D = 2$ and 5, and Kawatani *et al.* (1993) with $B/D = 5$ have also been plotted for comparison. Collectively, the results in this figure show a linear negative trend with increasing turbulence intensity, as discussed above. In comparison, the experimental data in the literature shows some deviation from a linear trend. As recorded by Kobayashi *et al.* (1992b), this could be attributed to signal noise for the acceleration - the numerical results do not suffer from such errors.

The results of the response amplitude for turbulence intensity (Fig.26(a)) provides a counter-intuitive relation between the response amplitude and turbulence intensity. Li and Melbourne (1995); Saathoff and Melbourne (1997); Li and Melbourne (1999); Daniels *et al.* (2013); Daniels (2016) have previously demonstrated that the presence of freestream turbulence increases the fluctuating surface pressure on a fixed geometry, which intuitively is expected to enhance the response amplitude. Clearly a different mechanism influences the resonant response of the structure. Considering effects of the integral length scales, it can be deduced that there is some correlation between the coherence of the freestream turbulence, MIV formation, and subsequently the structural response. More specifically, the freestream turbulence with increasing length scales in the tested range, must increase the strength of the MIV formed at the leading edge. Based on the analysis for the formation of the MIV in Daniels *et al.* (2016) and Nguyen *et al.* (2018), it can be deduced that the spanwise correlation of surface pressure is the result of MIV convecting along the cylinder which is affected by the freestream turbulence. To demonstrate this, Fig.27 shows iso-surfaces of vorticity around the cylinder at lock-in under smooth and turbulent flows. For the smooth flow, clearly a two-dimensional MIV is formed across the span resulting in a large correlation in pressure as it convects along the cylinder (see Daniels (2016); Daniels *et al.* (2016)), whereas for the turbulent case, the MIV breaks down due to the incoming

turbulence, diminishing the spanwise correlation of the surface pressure and subsequently the structural response.

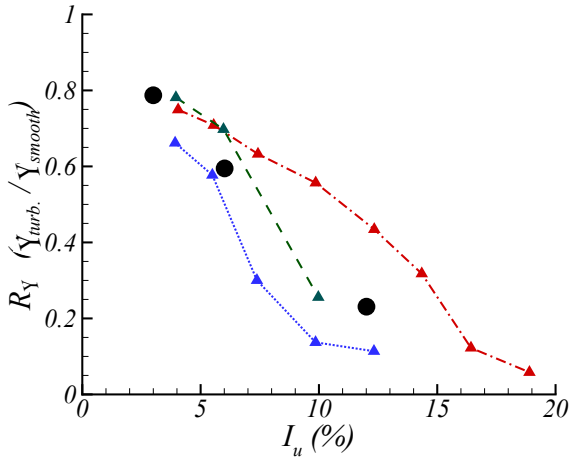

(a) Amplitude ratio versus turbulence intensity I_u.

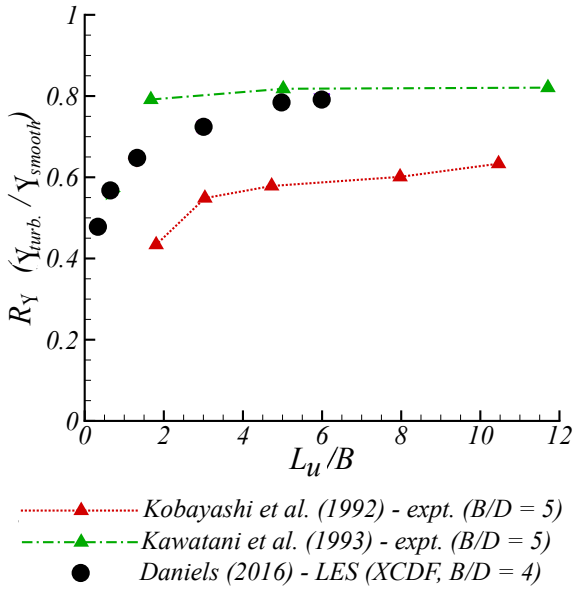

(b) Amplitude ratio versus integral length scale L_u.

Figure 26. Changes in the amplitude ratio between the smooth and turbulent flows with varying the turbulence intensity and length scales for the 1DOF heaving motion in the lock-in regime. Diagram source: Daniels (2016).

8. Closing remarks

A review is given for the application of Large-Eddy Simulation (LES) for the study of wind loading on an isolated high-rise building, and an aeroelastic responses of a long-span bridge.

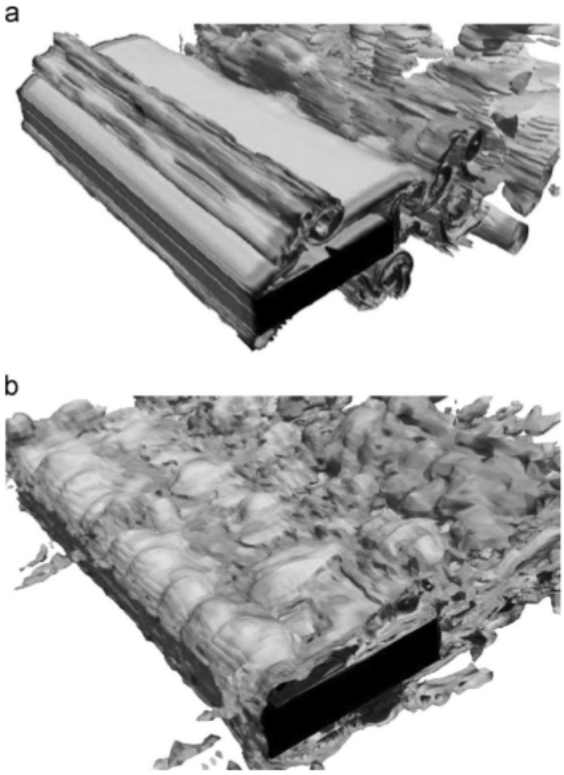

Figure 27. Instantaneous iso-surfaces of the vorticity magnitude $(-100, 100)$ (s^{-1}). Dynamic cases at lock-in (a) under smooth, (b) under turbulent flow. Diagram source: Daniels *et al.* (2016).

This review article discusses the available methods of inflow turbulence generation for LES. It should be noted that regardless of the inflow condition, the restriction of LES to model the higher frequencies in the von Kármán spectra forces the engineer to construct a reasonably fine grid. This becomes especially problematic when simulating an exact replica of the wind tunnel setup (or precursor method) to generate the inflow turbulence, making it an overall expensive (infeasible) choice of inflow methodology. The cheaper process of utilising a synthetic turbulence generation methodology is a bit more complicated than the remaining methods, since the domain is not built as an exact replica of a wind tunnel. Before the simulation to generate inflow turbulence, a decision should be made on what the key parameters are to be taken either from a wind tunnel experiment or from a field experiment. At present, most numerical simulations are performed as benchmark studies, where the key parameters are compared to wind tunnel tests. With increasingly better understanding in the natural atmospheric boundary layer, CFD techniques have the potential to simulate much greater Reynolds number flows than that of the wind tunnels, and simulate air-flows in more realistic meteorological conditions.

It is attractive to utilise a synthetic turbulence generation methodology, as it is more flexible and efficient than the other alternatives. The RFG method by Smirnov *et al.* (2001) is simply not adaptable for wind engineering studies, as it follows a Gaussian spectrum model. The DSRFG method by Huang *et al.* (2010) is utilised very often in comparison studies, and generally shows encouraging results. However, the method has been much criticised by researchers, resulting in a number of extensions for improving its accuracy and flexibility. The extended methods show improved results, though they have almost only been utilised by the researchers who proposed them. Hence none of these methods have yet been commonly used in wind engineering. The more recent digital-filtering method (XCDF) by Kim *et al.* (2013) shows very encouraging results at a potentially cheap cost. More recently developed synthetic turbulence generation methods are following the same trend (e.g. Bercin *et al.*, 2018). Nevertheless, despite the promising advances of inflow conditions for LES, it should be noted that the disparity of wind tunnel experimental data is quite large (Bruno. *et al.* (2014)), entailing a match between numerical and experimental results is not very hard to obtain, but not necessarily guarantee a true solution. At the same time, to explore the use of synthetic inflow generation methods in the future, the wind tunnel and field experiments need to provide more turbulence statistics, such as length scales.

The application of LES to estimating the resonant responses (and wind loading) of a long-span bridge section is still in its infancy. However, the scarce articles incorporating LES have made a number of significant contributions in providing a deeper insight into the flowfield and surface pressure during this process, whereas wind tunnel tests, to-date, have only provided speculations. These LES studies have ultimately identified the contributions of the Motion-Induced Vortex (e.g. Nguyen *et al.* (2018)) to the structure response amplitude. LES study ((e.g. Daniels *et al.*, 2016)) on the effect of freestream turbulence on fluid and structure interaction problems is only in its early stage, but is proved being a promising tool for this topic.

Overall, the results from the latest studies of high-rise buildings and long-span bridges are encouraging. In particular, the accuracy of numerical simulations has been largely improved, and the computational cost has been significantly reduced, owing to the fast advances of computer power and LES techniques. A best practice guide for LES to determine wind loads for structural design is still in high demand. Although CFD still needs wind tunnel validation, the numerical wind tunnel has already established itself as a very useful tool to make the architectural design phase more efficient. This entails that conventional wind tunnel tests are still necessary to perform for critical validations in the structural design. In nowadays both academic research and industrial projects, it is common that the numerical and experimental methods complement each other, and form a hybrid approach to carry out the work.

9. Acknowledgements

This project is supported by an EPSRC Case Ph.D. studentship: 1122 0726 and partly sponsored by Ove Arup and Partners Ltd. We thank Drs. Steven Downie and Ngai Yeung, and Mr. Andrew Allsop of Ove Arup and Partners Ltd for their support throughout. The computations were performed on the Iridis4, University of Southampton. S.J.D. is also grateful to Dr. Ender Ozkan of RWDI for his useful comments. Z.T.X. is grateful to the Met Office/UKRI funding support (Ref:CSSP China CHN 19/10) for preparing the MS.

REFERENCES

Aboshosha H, Elshaer A, Bitsuamlak G and Damatty AE (2015) Consistent inflow turbulence generator for LES evaluation of wind-induced responses for tall buildings. *Journal of Wind Engineering and Industrial Aerodynamics* **142**: 198–216, 10.1016/j.jweia.2015.04.004.

AIJ (2017) *Guidebook of Recommendations for Wind Loads on Buildings 2 - Wind Design (In Japanese). Technical report*, Architectural Institute of Japan, Tokyo, Japan.

Álvarez A, Nieto F, Nguyen D, Owen J and Hernández S (2019) 3D LES simulations of a static and vertically free-to-oscillate 4:1 rectangular cylinder: Effects of the grid resolution. *Journal of Wind Engineering and Industrial Aerodynamics* **192**: 31–44, 10.1016/j.jweia.2019.06.012.

Andrianne T (2012) *Experimental and numerical investigations of the aeroelastic stability of bluff bodies*. PhD thesis, Department of Aerospace and Mechanics, University of Liége, Liége, Belgium.

Bai YG, Yang K, Sun DK, Zhang YG, Kennedy D, Williams F and Gao XW (2013) Numerical aerodynamic analysis of bluff bodies at a high reynolds number with three-dimensional CFD modeling. *Science China Physics, Mechanics and Astronomy* **56(2)**: 277–289, 10.1007/s11433-012-4982-4.

Baines W (1963) Effects of velocity distribution on wind loads and flow patters on buildings. In *Symposium no.16, Wind Effects on Buildings and Structures* (London H, ed.), pp. 198–225.

Bearman P (1984) Vortex shedding from oscillating bluff bodies. *Annual Review of Fluid Mechanics* **16**: 195–222, 10.1017/S0022112080000596.

Bercin K, Xie ZT and Turnock R (2018) Exploration of digital-filter and forward-stepwise synthetic turbulence generators and an improvement for their skewness-kurtosis. *Computers & Fluids* **172**: 443–466, 10.1016/j.compfluid.2018.03.070.

Bi A (2006) *Probability assessment of wind loads on a full scale low rise building*. PhD thesis, Texas Tech University, Lubbock, Texas, United States.

Billson M, Eriksson LE, Davidson L and Jordan P (2004) Modeling of synthesized anisotropic turbulence and its sound emission. In *Collection of Technical Papers - 10th AIAA/CEAS Aeroacoustics Conference*, vol. 1, 10.2514/6.2004-2857.

Blocken B (2014) 50 years of Computational Wind Engineering: past, present and future. *Journal of Wind Engineering and Industrial Aerodynamics* **129**: 69–102, 10.1016/j.jweia.2014.03.008.

Blocken B and Gualtieri C (2012) Ten iterative steps for model development and evaluation applied to Computational Fluid Dynamics for environmental fluid mechanics. *Environmental Modelling Software* **33**: 1–22, 10.1016/j.envsoft.2012.02.001.

Breton SP, Sumner J, Soresnen J, Hansen K, Sarmast S and Ivanell S (2017) A survey of modelling methods for high-fidelity wind farm simulations using large-eddy simulation. *Philosophical Transactions of The Royal Society A Mathematical Physical and Engineering Sciences* **375(2091)**: 46 – 50, 10.1098/rsta.2016.0097.

Bruno L, Coste N and Fransos D (2012) Simulated flow around a rectangular 5:1 cylinder: Spanwise discretisation effects and emerging flow features. *Journal of Wind Engineering and Industrial Aerodynamics* **106**: 203–215, 10.1016/j.jweia.2012.03.018.

Bruno L, Fransos D, Coste N and Bosco A (2010) 3D flow around a rectangular cylinder: A computational study. *Journal of Wind Engineering and Industrial Aerodynamics* **98**: 263–276, 10.1016/j.jweia.2009.10.005.

Bruno. L, Salvetti. M and Ricciardelli F (2014) Benchmark on the aerodynamics of a rectangular 5:1 cylinder: an overview after the first four years of activity. *Journal of Wind Engineering and Industrial Aerodynamics* **126**: 87–106, 10.1016/j.jweia.2014.01.005.

Cao S, and Cao J (2017) Toward better understanding of turbulence effects on bridge aerodynamics. *Frontiers in Built Environment* **3**: 72, 10.3389/fbuil.2017.00072.

Capra S, Cammelli S, Roeder D and Knir J (2018) Numerically simulated wind loading on a high-rise structure and its correlation with experimental wind tunnel testing. In *The Seventh International Symposium on Computational Wind Engineering (CWE2018)*, Seoul, Republic of Korea, pp. 154–155.

Castro G, Paz R and Sonzogni V (2011) Generation of turbulence inlet velocity conditions for Large-Eddy Simulation. *Laboratorio de Mecánica Computacional* **30**: 2275–2288.

Chen Y, Djidjeli K and Xie ZT (2019) Large eddy simulation of flow past stationary and oscillating square cylinders. *Journal of Fluids and Structures* **under review**.

Cochran L and Derickson R (2011) A physical modelers view of computational wind engineering. *Journal of Wind Engineering and Industrial Aerodynamics* **99**: 139–153, 10.1016/j.jweia.2011.01.015.

Cochran. L, Derickson. R, Meroney. R and Sharp H (2015) On what new building project managers need to know about wind engineering. In *17th Australasian Wind Engineering Society Workshop*, Wellington, New Zealand.

Dagnew A and Bitsuamlak G (2009) Computational evaluation of wind pressures on tall buildings. 11th Americas Conference on Wind Engineering, San Juan, Puerto Rico, pp. 1–17.

Dagnew A and Bitsuamlak G (2010) LES evaluation of wind pressures on a standard tall building with and without a neighbouring building. In *The Fifth International Symposium on Computational Wind Engineering (CWE2010)*, Chapel Hill, North Carolina, USA, pp. 23–27.

Dagnew A and Bitsuamlak G (2013) Computational evaluation of wind loads on buildings: A review. *Wind and Structures* **16(6)**: 629–660, 10.12989/was.2013.16.6.629.

Dagnew A and Bitsuamlak G (2014) Computational evaluation of wind loads on a standard tall building using LES. *Wind and Structures* **18(5)**: 567–598, 10.12989/was.2014.18.5.567.

Daniels S (2016) *An Evaluation of Vortex Shedding over Slender Structures using Large-Eddy Simulation*. PhD thesis, University of Southampton, UK.

Daniels S, Castro I and Xie ZT (2013) Peak loading and surface pressure fluctuations of a tall model building. *Journal of Wind Engineering and Industrial Aerodynamics* **120**: 19–28, 10.1016/j.jweia.2013.06.014.

Daniels S, Castro I and Xie ZT (2016) Numerical analysis of freestream turbulence effects on the vortex-induced vibrations of a rectangular cylinder. *Journal of Wind Engineering and Industrial Aerodynamics* **153**: 13–25, 10.1016/j.jweia.2016.03.007.

Daniels S and Xie ZT (2015) Free-stream turbulence effects on long-span bridge aerodynamics. *Procedia Engineering* **126**: 199–203, 10.1016/j.proeng.2015.11.218, frontiers in Fluid Mechanics Research.

Davenport A (1960) Rationale for determining design wind velocities. *Journal of the structural division: American society of Civil Engineers* **86**: 39–68.

di Mare L, Klein M, Jones W and Janicka J (2006) Synthetic turbulence inflow conditions for large-eddy simulation. *Journal of Physics of Fluids* **18(2)**: 1–11, 10.1063/1.2130744.

Diana G, Fiammenghi G, Belloli M and Rocchi D (2013) Wind tunnel tests and numerical approach for long span bridges: The messina bridge. *Journal of Wind Engineering and Industrial Aerodynamics* **122**: 38 – 49, https://doi.org/10.1016/j.jweia.2013.07.012, the Seventh International Colloquium on Bluff Body Aerodynamics and Applications (BBAA7).

Elshaer A, Aboshosha H, Bitsuamlak G, Damatty AE and Dagnew A (2016) LES evaluation of wind-induced responses for an isolated and a surrounded tall building. *Engineering Structures* **115**: 179–195, 10.1016/j.engstruct.2016.02.026.

Eurocode (2005) *Eurocode 1: actions on structures - Part 1-4: General actions - wind actions. Technical Report 85020*, Engineering Sciences Data Unit (ESDU).

Eurocode (2011) *Integral length scales of turbulence over flat terrain with roughness changes*. *Technical Report 86035*, Engineering Sciences Data Unit (ESDU).

Germano M, Piomelli U, Moin P and Cabot WH (1991) A dynamic subgrid-scale eddy viscosity model. *Physics of Fluids A* **3(7)**: 1760–1765, 10.1063/1.857955.

Goliger A and Milford R (1988) Sensitivity of the CAARC standard building model to geometric scale and turbulence. *Journal of Wind Engineering and Industrial Aerodynamics* **31(1)**: 105–123, 10.1016/0167-6105(88)90190-0.

Goswami I, Scanlan R and Jones N (1993) Vortex-induced vibration of circular cylinders i: Experimental data. *Journal of Engineering Mechanics* **11**: 2270–2287, 10.1061/(ASCE)0733-9399(1993)119:11(2270).

Guissart A, Andrianne T, Dimitriadis G and Terrapon V (2019) Numerical and experimental study of the flow around a 4:1 rectangular cylinder at moderate reynolds number. *Journal of Wind Engineering and Industrial Aerodynamics* **189**: 289–303, 10.1016/j.jweia.2019.03.026.

Haan F (2000) *The effects of turbulence on the aerodynamics of long-span bridges*. PhD thesis, University of Notre Dame, Department of Aerospace and Mechanical Engineering, Indiana, United States.

Hansen S (2013) Vortex-induced vibrations – the scruton number revisited. *Proceedings of the Institution of Civil Engineers – Structures and Buildings* **166(10)**: 560–571, 10.1680/stbu.11.00018.

Holmes J (2014) Along and cross-wind response of a generic tall building: comparison of wind-tunnel data with codes and standards. *Journal of Wind Engineering and Industrial Aerodynamics* **132**: 136–141, 10.1016/j.jweia.2014.06.022.

Huang P, Luo P and Gu M (2005) Pressure and forces measurements on CAARC standard tall building in wind tunnel of tongji university. 12th National Wind Engineering Conference of China, Xi'an, China, pp. 240–244.

Huang S, Li Q and Wu J (2010) A general inflow turbulence generator for large-eddy simulation. *Journal of Wind Engineering and Industrial Aerodynamics* **98(10–11)**: 600–617, 10.1016/j.jweia.2010.06.002.

Huang S, Li Q and Xu S (2007) Numerical evaluation of wind effects on a tall steel building by CFD. *Journal of Constructional Steel Research* **63(5)**: 612–627, 10.1016/j.jcsr.2006.06.033.

Irwin P (2009) Wind engineering challenges of the new generation of super-tall buildings. *Journal of Wind Engineering and Industrial Aerodynamics* **97(7–8)**: 328–334.

Jaiman R, Geubelle P, Loth E and Jiao X (2011) Transient fluid-structure interaction with non-matching spatial and temporal discretizations. *Computers % Fluids* **50(1)**: 120–135, 10.1016/j.compfluid.2011.07.001.

Jamal H and Dalton C (2005) The contrast in phase angles between forced and self-excited oscillations of a circular cylinder. *Journal of Fluids and Structures* **20**: 467–482, 10.1016/j.jfluidstructs.2005.02.001.

Jensen M (1958) The model law for phenomena in the natural wind. *Ingeni. International Edition 2* .

Jø rgensen N, Koss H and Bennetsen G (2014) LES and experiment of turbulent boundary layer flow around a floor-mounted cube. In *The Sixth International Symposium on Computational Wind Engineering (CWE2014)*, Hamburg, Germany, pp. 76–77.

Kareem A and Wu T (2013) Wind-induced effects on bluff bodies in turbulent flows: Nonstationary, non-gaussian and nonlinear features. *Journal of Wind Engineering and Industrial Aerodynamics* **122**: 21–37, https://doi.org/10.1016/j.jweia.2013.06.002, the Seventh International Colloquium on Bluff Body Aerodynamics and Applications (BBAA7).

Kataoka H and Mizuno M (2002) Numerical flow computation around aeroelastic 3d square cylinder using inflow turbulence. *Wind and Structures* **5(2-3-4)**: 379–392, 10.12989/WAS.2002.5.2_3_4.379.

Kawatani M, Kim H, Uejima H and Kobayashi H (1993) Effects of turbulent flows on vortex-induced oscillation of bridge girders with basic sections. *Journal of Wind Engineering and Industrial Aerodynamics* **49**: 477–486, 10.1016/0167-6105(93)90042-M.

Kawatani M, Toda N, Sato M and Kobayashi H (1999) Vortex-induced torsional oscillations of bridge girders with basic sections in turbulent flows. *Journal of Wind Engineering and Industrial Aerodynamics* **83**: 327–336, 10.1016/S0167-6105(99)00082-3.

Kim Y, Castro I and Xie ZT (2013) Divergence-free turbulence inflow conditions for large-eddy simulations with incompressible flow solvers. *Computers & Fluids* **84**: 56–68, 10.1016/j.compfluid.2013.06.001.

Kim Y and Xie ZT (2016) Modelling the effect of freestream turbulence on dynamic stall of wind turbine blades. *Computers & Fluids* **129**: 53–66, 10.1016/j.compfluid.2016.02.004.

Klein M, Sadiki A and Janicka J (2003) A digital filter based generation of inflow data for spatially developing direct numerical or large-eddy simulations. *Journal of Computers and Physics* **186**: 652–665, 10.1016/S0021-9991(03)00090-1.

Kobayashi H, Kawatani M and Kim H (1992a) Effects of turbulence characteristics on vortex-induced oscillation of rectangular cylinders. *Journal of Wind Engineering and Industrial Aerodynamics* **41-44**: 775–784, 10.1016/0167-6105(92)90496-W.

Kobayashi H, Kawatani M and Kim H (1992b) Effects of turbulence characteristics on vortex-induced oscillation of rectangular

cylinders. *Journal of wind engineering and industrial aerodynamics* **41-44**: 775–784, 10.1016/0167-6105(92)90496-W.

Kobayashi H, Kawatani M and Nakade O (1990) Vortex-induced oscillation of two dimensional rectangular cylinders in large scale turbulence. *Journal of Wind Engineering and Industrial Aerodynamics* **33**: 101–106, 10.1016/0167-6105(90)90025-8.

Komatsu S and Kobayashi H (1980) Vortex-induced oscillation of bluff cylinders. *Journal of Wind Engineering and Industrial Aerodynamics* **6(3-4)**: 335–362, 10.1016/0167-6105(80)90010-0.

Kraichnan R (1970) Diffusion by a random velocity field. *Journal of Physics of Fluids* **11**: 21–31, 10.1063/1.1692799.

Lamberti G, Garcia-Sánchez C, Sousa J and Gorlé C (2018) Optimizing turbulent inflow conditions for large-eddy simulations of the atmospheric boundary layer. *Journal of Wind Engineering and Industrial Aerodynamics* **177**: 32–44, 10.1016/j.jweia.2018.04.004.

Larson A and Larose G (2015) Dynamic wind effects on suspension and cable-stayed bridges. *Journal of Sound and Vibration* **334**: 2–28, 10.1016/j.jsv.2014.06.009.

Li Q and Melbourne W (1995) An experimental investigation of the effects of free-stream turbulence on streamwise surface pressures in separated and reattaching flows. *Journal of Wind Engineering and Industrial Aerodynamics* **54/55**: 313–323, 10.1016/0167-6105(94)00050-N.

Li Q and Melbourne W (1999) The effect of large-scale turbulence on pressure fluctuations in separated and reattaching flows. *Journal of Wind Engineering and Industrial Aerodynamics* **83**: 159–169, 10.1016/S0167-6105(99)00069-0.

Lund T, Wu X and Squires K (1998) Generation of turbulent inflow data for spatially-developing boundary layer simulations. *J. Comput. Phys.* **140**: 233–258, 10.1006/jcph.1998.5882.

Mannini C, Mariotti A, Siconolfi L and Salvetti MV (2019) Benchmark on the aerodynamics of a 5:1 rectangular cylinder: Further experimental and LES results. In *Direct and Large-Eddy Simulation XI* (Salvetti M, Armenio V, Fröhlich J, Geurts B and Kuerten H, eds), Springer International Publishing, Cham, pp. 427–432.

Mannini C, Marra A and Bartoli G (2014) VIV-Galloping instabilty of rectangular cylinders: review and new experiments. *Journal of Wind Engineering and Industrial Aerodynamics* **132**: 109–124, 10.1016/j.jweia.2014.06.021.

Mannini C, Marra A, Pigolotti L and Bartoli G (2017) The effects of free-stream turbulence and angle of attack on the aerodynamics of a cylinder with rectangular 5:1 cross section. *Journal of Wind Engineering and Industrial Aerodynamics* **161**: 42–58, 10.1016/j.jweia.2016.12.001.

Marra A (2011) *Risk assessment of bridge decks prone to Vortex Induced Vibrations*. PhD thesis, Department of Architecture, Civil Engineering and Environmental Sciences, University of Braunschweig – Institute of Technology, Germany.

Marra A, Mannini C and Bartoli G (2011) Van der Pol-type equation for modeling vortex-induced oscillations of bridge decks. *Journal of Wind Engineering and Industrial Aerodynamics* **99**: 776–785, 10.1016/j.jweia.2011.03.014.

Marra A, Mannini C and Bartoli G (2015) Measurements and improved model of vortex-induced vibration for an elongated rectangular cylinder. *Journal of Wind Engineering and Industrial Aerodynamics* **147**: 358–367, 10.1016/j.jweia.2015.08.007.

Martinuzzi R and Havel B (2000) Turbulent flow around two interfering surface mounted cubic obstacles in tandem arrangement. *Journal of Fluids Engineering* **122**: 24–31, 10.1115/1.483222.

Marzouk OA (2011) One-way and two-way couplings of cfd and structural models and application to the wake-body interaction. *Journal of Applied Mathematical Modelling* **35**: 1036–1053, 10.1016/j.apm.2010.07.049.

Mathey F, Cokljat D, Bertoglio JP and Sergent E (2006) Assessment of the vortex method for Large-Eddy Simulation inlet conditions. *Progress in Computational Fluid Dynamics - PROG COMPUT FLUID DYN* **6**, 10.1504/PCFD.2006.009483.

Matsumoto M (1996) Aerodynamic damping of prisms. *Journal of Wind Engineering and Industrial Aerodynamics* **59**: 159–197, 10.1016/0167-6105(96)00005-0.

Matsumoto M (2009) Vortex effect on torsional flutter. In *The seventh Asia-Pacific conference on wind engineering*, APCWE-VII, Taipei, Taiwan.

Matsumoto M, Shiraishi N, Stoyanoff S and Yagi T (1993) Mechanism of, and turbulence effect on vortex-induced oscillations for bridge box girders. *Journal of Wind Engineering and Industrial Aerodynamics* **49(1-3)**: 467–476, 10.1016/0167-6105(93)90041-L.

Matsumoto M, Shirato H, Yagi T, Shijo R, Eguchi A and Tamaki H (2003) Effects of aerodynamic interferences between heaving and torsional vibration of bridge decks: the case of the tacoma narrows bridge. *Journal of Wind Engineering and Industrial Aerodynamics* **91**: 1547–1557, 10.1016/j.jweia.2003.09.010.

Matsumoto M, Yagi T, Tamaki H and Tsubota T (2008) Vortex-Induced Vibration and its effect on torsional flutter instability in the case of B/D = 4 rectangular cylinder. *Journal of Wind Engineering and Industrial Aerodynamics* **96**: 971–983, 10.1016/j.jweia.2007.06.023.

Melbourne W (1979) Turbulence effects on maximum surface pressures - a mechanism and possibility of reduction. In *5th International Conference on Wind Engineering*, vol. 1, Fort Collins, Colorado, USA, pp. 541–551, 10.1016/B978-1-4832-8367-8.50055-3.

Melbourne WH (1980) Comparison of measurements on the CAARC standard tall building model in simulated model wind flows. *Journal of Wind Engineering and Industrial Aerodynamics* **6(1–2)**: 73–88, 10.1016/0167-6105(80)90023-9.

Meroney R (2016) Ten questions concerning hybrid computational/physical model simulation of wind flow in the built environment. *Building and Environment* **96**: 12–21, 10.1016/j.buildenv.2015.11.005.

Mills R, Sheridan J and Hourigan K (2002) Response of base suction and vortex shedding from rectangular prisms to transverse forcing. *Journal of Fluid Mechanics* **461**: 25–49, 10.1017/S0022112002008534.

Nakamura Y and Mizota T (1975) Torsional flutter of rectangular prisms. *Journal of the Engineering Mechanics Division ASCE* **(no. EM2)**: 125–142.

Naudascher E and Wang Y (1993) Flow-induced vibrations of prismatic bodies and grids of prisms. *Journal of Fluids and Structures* **7**: 341–373, 10.1006/jfls.1993.1021.

Nguyen DT, Hargreaves D and Owen J (2018) Vortex-Induced Vibration of a 5:1 rectangular cylinder: A comparison of wind tunnel sectional model tests and computational simulations. *Journal of Wind Engineering and Industrial Aerodynamics* **175**: 1–16, 10.1016/j.jweia.2018.01.029.

Nicoud F and Ducros F (1999) Subgrid-scale modelling based on the square of the velocity gradient tensor. *Flow, Turbulence and Combustion* **62**: 183–200, 10.1023/A:1009995426001.

Nozawa K and Tamura T (2002) Large-Eddy Simulation of the flow around a low-rise building immersed in a rough-wall turbulent boundary layer. *Journal of Wind Engineering and Industrial Aerodynamics* **90**: 1151–1162, 10.1016/S0167-6105(02)00228-3.

Nozu T, Tamura T, Takeshi K and Akira K (2015) Mesh-adaptive LES for wind load estimation of a high-rise building in a city. *Journal of Wind Engineering and Industrial Aerodynamics* **144**: 62–69, 10.1016/j.jweia.2015.05.007.

Okaze T and Mochida A (2017) Cholesky decomposition-based generation of artificial inflow turbulence including scalar fluctuation. *Computers & Fluids* **159**: 23–32, 10.1016/j.compfluid.2017.09.005.

Owen J, Sterling M, Hargreaves D and Baker C (2013) *Fifty years of wind engineering: prestige lectures from the sixth European and African conference on wind engineering*. University of Birmingham, UK.

Patruno L, Ricci M, de Miranda S and Ubertini F (2016) Numerical simulation of a 5:1 rectangular cylinder at non-null angles of attack. *Journal of Wind Engineering and Industrial Aerodynamics* **151**: 146 – 157, 10.1016/j.jweia.2016.01.008.

Phuc P, Nozu T, Kikuchi H and Hibi K (2012) A large-scale simulation on CFD in construction industry. *TSUBAME ESJ. - Global Scientific Information and Computing Center* **8**: 17–22.

Phuc P, Nozu T, Kikuchi H, Hibi K and Tamura Y (2014) A numerical study on wind pressure on a building with a setback using Large Eddy Simulation. In *The Sixth International Symposium on Computational Wind Engineering (CWE2014)*, Hamburg, Germany, pp. 154–155.

Placzek A, Sigrist R and Hamdouni A (2008) Numerical simulation of an oscillating cylinder in cross-flow at low reynolds number: forced and free oscillations. *Computers & Fluids* **38**: 80–100, 10.1016/j.compfluid.2008.01.007.

Pope S (2000) *Turbulent Flows*. Cambridge University Press; 1st edition.

Ricci M, Patruno L, de Miranda S and Ubertini F (2017) Flow field around a 5:1 rectangular cylinder using LES: Influence of inflow turbulence conditions, spanwise domain size and their interaction. *Computers & Fluids* **149**: 181 – 193, 10.1016/j.compfluid.2017.03.010.

Ricciardelli F (2010) Effects of vibration regime on the spanwise correlation of the aerodynamics forces on a 5:1 rectangular cylinder. *Journal of Wind Engineering and Industrial Aerodynamics* **98**: 215–225, 10.1016/j.jweia.2009.10.017.

Ricciardelli F, de Grenet E and Hangan H (2002) Pressure distribution, aerodynamic forces and dynamic response of box bridge sections. *Journal of Wind Engineering and Industrial Aerodynamics* **90**: 1135–1150, 10.1016/S0167-6105(02)00227-1.

Saathoff P and Melbourne W (1997) Effects of free-stream turbulence on surface pressure fluctuations in a separation bubble. *Journal of Fluid Mechanics* **337**: 1–24, 10.1017/S0022112096004594.

Sarwar M and Ishihara T (2010) Numerical study on suppression of Vortex-Induced Vibrations of box girder bridge section by aerodynamic countermeasures. *Journal of Wind Engineering and Industrial Aerodynamics* **98**: 701–711, 10.1016/j.jweia.2010.06.001.

Sarwar M, Ishihara T, Shimada K, Tamasaki Y and Ikeda T (2008) Prediction of aerodynamic characteristics of a box girder bridge section using the LES turbulence model. *Journal of Wind Engineering and Industrial Aerodynamics* **96**: 1895–1911, 10.1016/j.jweia.2008.02.015.

Sau A, Hwang R, Sheu T and Yang W (2003) Interaction of trailing vortices in the wake of a wall-mounted rectangular cylinder. *Physical Review, Series E* **68(5)**, 10.1103/PhysRevE.68.056303.

Shimada K and Ishihara T (2002) Application of a modified $k-\epsilon$ model to the prediction of aerodynamic characteristics of rectangular cross-section cylinders. *Journal of Fluids and Structures* **16**: 465–485, 10.1006/jfls.2001.0433.

Shimada K and Ishihara T (2012) Predictability of unsteady two-dimensional k-ϵ model on the aerodynamics instabilities of some rectangular prisms. *Journal of Fluids and Structures* **28**: 20–39, 10.1016/j.jfluidstructs.2011.08.013.

Shiraishi N and Matsumoto M (1983) On classification of vortex-induced oscillation and its application for bridge structures. *Journal of Wind Engineering and industrial Aerodynamics* **14(1-3)**: 419–430, 10.1016/0167-6105(83)90043-0.

Simiu E and Scanlan R (1978) *Wind effects on structures*. John Wiley and Sons.

Smagorinsky J (1963) General circulation experiments with the primitive equations. *Monthly Weather Review* **91(3)**: 99–164, 10.1175/1520-0493(1963)091<0099:GCEWTP>2.3.CO;2.

Smirnov A, Shi S and Celik I (2001) Random flow generation technique for Large-Eddy Simulations and particle-dynamics modeling. *Journal of Fluids Engineering* **123**: 359–71, 10.1115/1.1369598.

Stevens R, Graham J and Meneveau C (2014) A concurrent precursor inflow method for Large-Eddy Simulations and applications to finite length wind farms. *Renewable Energy* **68**: 46 – 50, 10.1016/j.renene.2014.01.024.

Stull RB (1988) *An Introduction to Boundary Layer Meteorology*. Kluwer Academy Publication, Dordrecht, Boston, London.

Sun D, Owen J and Wright N (2009) Application of the k-ω turbulence model for a wind-induced vibration study of 2D bluff bodies. *Journal of Wind Engineering and Industrial Aerodynamics* **97**: 77–87, 10.1016/j.jweia.2008.08.002.

Sun D, Owen J, Wright N and Liaw K (2008) Fluid–structure interaction of prismatic line-like structures, using LES and block-iterative coupling. *Journal of Wind Engineering and Industrial Aerodynamics* **96**: 840–858, 10.1016/j.jweia.2007.06.012.

Tabor G and Baba-Ahmadi M (2010) Inlet conditions for Large-Eddy Simulation: A review. *Computers & Fluids* **39(4)**: 553–567, 10.1016/j.compfluid.2009.10.007.

Tamura T, Nozawa K and Kondo K (2008) AIJ guide for numerical prediction of wind loads on buildings. *Journal of Wind Engineering and Industrial Aerodynamics* **96(10-11)**: 1974–1984, 10.1016/j.jweia.2008.02.020.

Thordal M, Bennetsen J, Holger H and Koss H (2019) Review for practical application of CFD for the determination of wind load on high-rise buildings. *Journal of Wind Engineering and Industrial Aerodynamics* **186**: 155–168, 10.1016/j.jweia.2018.12.019.

Tieleman H (1993) Wind loads on roofs of low-rise structures. In *ASCE Conference*, Miami, Florida, USA.

Utsunomiya H, Nagao F, Nodea M and Tanaka E (2001) Vortex-induced oscillation of a bridge in slowly fluctuating wind. *Journal of Wind Engineering and Industrial Aerodynamics* **89**: 1689–1699, 10.1016/S0167-6105(01)00131-3.

van Driest ER (1956) On turbulent flow near a wall. *AIAA* **23**: 1007–1011, 10.2514/8.3713.

Vandiver J, Cheng Y, Jaiswal V, Sheshadri A and Yu A (2009) An experimental evaluation of Vortex -Induced Vibration of a riser bundle with gaps. In *Proceedings of the ASME 2009 28th International Conference on Ocean, Offshore and Arctic Engineering*, pp. 695–705, 10.1115/OMAE2009-79757.

Wang H, Zhouo Y, Chan C, Wong W and Lam K (2004) Flow structure around a finite length square prism. 15th Australasian Fluid Mechanics Conference, University of Sydney, Australia.

Wang W and Zhou Y (2009) The finite length square cylinder near wake. *Journal of Fluid Mechanics* **18**: 453–490, 10.1017/S0022112009990693.

Wardlaw R (1980) Sectional versus full model wind tunnel testing of bridge road decks. In *Proceedings of the Indian Academy of Sciences*, vol. 3, pp. 177–198.

Wingstedt E, Osnes A, Åkervik E, Eriksson D and Reif BP (2017a) Large-eddysimulation of dense gas dispersion over a simplified urban area. *Atmos.Environ.* **152**: 605–616, 10.1016/j.atmosenv.2016.12.039.

Wingstedt E, Vartdal M and Reif BP (2017b) Large-eddy simulations of dense-gasdispersion within a high-reynolds number turbulent boundary layer. *Phys. Fluids* **29**: 605–616, 10.1063/1.499946629.

Wu T and Kareem A (2012) An overview of vortex-induced vibration (VIV) of bridge decks. *Frontiers of Structural Civil Engineering* **6(4)**: 335–347, 10.1007/s11709-012-0179-1.

Wu X (2017) Inflow turbulence generation methods. *Annual Review of Fluid Mechanics* **49(1)**: 23–49, 10.1146/annurev-fluid-010816-060322.

Xie ZT and Castro I (2008a) Efficient generation of inflow conditions for Large-Eddy Simulation of street-scale flows. *Journal of Flow, Turbulence and Combustion* **81(3)**: 449–470, 10.1007/s10494-008-9151-5.

Xie ZT and Castro IP (2008b) Efficient generation of inflow conditions for large eddy simulation of street-scale flow. *Journal of Flow, and Turbulent Combustion* **81**: 449–470, 10.1007/s10494-008-9151-5.

Yan B and Li Q (2015) Inflow turbulence generation methods with Large-Eddy Simulation for wind effects on tall buildings. *Computers & Fluids* **116**: 158–175, 10.1016/j.compfluid.2015.04.020.

Yazdi J, Sarkardeh H, Azamathulla H and Ghani A (2010) 3d simulation of flow around a single spur dike with free-surface flow. *International Journal of River Basin Management* **8(1)**: 55–62, 10.1080/15715121003715107.

Yoshikawa M and Tamura T (2012) LES for wind load estimation by unstructured grid system. In *The Seventh International Colloquium on Bluff Body Aerodynamics and Applications (BBAA7)*, Shanghai, China, pp. 1960–1965.

Yoshikawa M and Tamura T (2013) LES of fluctuating pressures on a high-rise building influenced by windward building. In *The Eighth Asia-Pacific Conference on Wind Engineering*

(APCWE-VIII), Chennai, India, pp. 572–581.

Zhang Y, Habashi W and Khurram R (2015) Predicting wind-induced vibrations of high-rise buildings using unsteady CFD and modal analysis. *Journal of Wind Engineering and Industrial Aerodynamics* **136**: 165—179, 10.1016/j.jweia.2014.11.008.

Zhu Z and Chen Z (2013) Large-Eddy Simulation of aerodynamics of a flat box girder on long-span bridges. *Procedia Engineering* **61**: 212–219, 10.1016/j.proeng.2013.08.006, 25th International Conference on Parallel Computational Fluid Dynamics.